Hinchliffe, P., Gonzalez, M. M., Mojica, M. F., Gonzalez, J. M., Castillo, V., Saiz, C., Kosmopoulou, M., Tooke, C., Llarrull, L., Mahler, G., Bonomo, R. A., Villa, A. J., & Spencer, J. (2016). Cross-class metallo-β-lactamase inhibition by bisthiazolidines reveals multiple binding modes. *Proceedings of the National Academy of Sciences of the United States of America*, *113*(26), E3745-E3754. https://doi.org/10.1073/pnas.1601368113

Short title: Cross-class metallo-β-lactamase inhibitors

Cross-class metallo-β-lactamase inhibition by bisthiazolidines reveals multiple binding modes

Philip Hinchliffe[a], Mariano M. González[b], Maria F. Mojica[c], Javier M. González[d], Valerie Castillo[e], Cecilia Saiz[e], Magda Kosmopoulou[a], Catherine L. Tooke[a], Leticia I. Llarrull[b], Graciela Mahler[e], Robert A. Bonomo[c], Alejandro J. Vila[b,1], James Spencer[a,1]

[1]*To whom correspondence should be addressed:* Email: vila@ibr-conicet.gov.ar or Jim.Spencer@bristol.ac.uk

[a]School of Cellular and Molecular Medicine, Biomedical Sciences Building, University of Bristol, University Walk, Bristol BS8 1TD, United Kingdom

[b]Instituto de Biología Molecular y Celular de Rosario (IBR-CONICET), Facultad de Ciencias Bioquímicas y Farmacéuticas, Universidad Nacional de Rosario (UNR), Ocampo y Esmeralda, 2000 Rosario, Argentina

[c]Research Service, Louis Stokes Cleveland Department of Veterans Affairs Medical Center, and Departments of Pharmacology, Biochemistry, Microbiology, and Molecular Biology, Case Western Reserve University, Cleveland, Ohio 44106, United States

[d]Instituto de Bionanotecnología, INBIONATEC-CONICET. Universidad Nacional de Santiago del Estero (UNSE), RN 9, Km 1125, G4206XCP Santiago del Estero, Argentina

[e]Laboratorio de Química Farmacéutica, Facultad de Química, Universidad de la República (UdelaR), Montevideo 11800, Uruguay

Data deposition: The atomic coordinates and structure factors have been deposited in the Protein Data Bank, www.pdb.org with PDB ID codes 5EWA (IMP-1:**2a**), 5EW0 (Sfh-I:**1a**), 5EV6 (IMP-1, native), 5EV8 (IMP-1:**1b**), 5EVB (L1:**1b**), 5EVD (L1:**2b**), 5EVK (L1:**1a**) and 4NQ6 (BcII:**1b**).

Keywords: carbapenemase, antibiotic resistance, inhibitors, bisthiazolidines, metallo-β-lactamase, broad-spectrum

Author contributions: P.H., L.I.L., G.M., R.A.B., A.J.V., and J.S. designed research; P.H., M.M.G., M.M., J.M.G., V.C., C.S., M.K., and C.L.T. performed research; P.H., M.M.G., M.M., J.M.G., L.I.L., G.M., R.A.B., A.J.V., and J.S. analyzed data; and, P.H., L.I.L., G.M., R.A.B., A.J.V., and J.S. wrote the paper.

Classification: BIOLOGICAL SCIENCES: Microbiology

Abstract

Metallo-β-lactamases (MBLs) hydrolyze almost all β-lactam antibiotics and are unaffected by clinically available β-lactamase inhibitors (βLIs). Active-site architecture divides MBLs into three classes (B1, B2 and B3), complicating development of βLIs effective against all enzymes. Bisthiazolidines (BTZs) are carboxylate-containing, bicyclic compounds, considered as penicillin analogues with an additional free thiol. Here, we show both L- and D-BTZ enantiomers are micromolar competitive βLIs of all MBL classes in vitro, with K_is of 6-15 μM or 36-84 μM for subclass B1 MBLs (IMP-1 and BcII, respectively), and 10-12 μM for the B3 enzyme L1. Against the B2 MBL Sfh-I, the L-BTZ enantiomers exhibit 100-fold lower K_is (0.26-0.36 μM) than D-BTZs (26-29 μM). Importantly, cell-based time-kill assays show BTZs restore β-lactam susceptibility of *E. coli* producing MBLs (IMP-1, Sfh-1, BcII and GOB-18) and, significantly, an extensively drug resistant *Stenotrophomonas maltophilia* clinical isolate expressing L1. These data therefore show BTZs to inhibit the full range of MBLs, and potentiate β-lactam activity against producer pathogens. X-ray crystal structures reveal insights into diverse BTZ binding modes, varying with orientation of the carboxylate and thiol moieties. BTZs bind the di-zinc centers of B1 (IMP-1; BcII) and B3 (L1) MBLs via the free thiol, but orient differently depending upon stereochemistry. In contrast, the L-BTZ carboxylate dominates interactions with the monozinc B2 MBL Sfh-I, with the thiol uninvolved. D-BTZ complexes most closely resemble β-lactam binding to B1 MBLs, but feature an unprecedented disruption of the D120-zinc interaction. Cross-class MBL inhibition therefore arises from the unexpected versatility of BTZ binding.

Significance statement

Bacterial diseases remain a huge burden on healthcare worldwide, with the emergence and re-emergence of strains resistant to currently used antibiotics posing an increasing clinical threat. Metallo-β-lactamases (MBLs) are key determinants of antibiotic resistance as they hydrolyze almost all β-lactam antibiotics and are unaffected by currently available β-lactamase inhibitors (βLIs). The structural diversity between MBLs has proved problematic when designing βLIs effective against all MBL targets. Here we show a series of small compounds, bisthiazolidines, to act as inhibitors of all MBL types, restoring the efficacy of currently used antibiotics against resistant bacterial strains producing different MBLs. High-resolution crystal structures reveal how diverse MBLs are inhibited by the unexpected versatility of bisthiazolidine binding, raising implications for future βLI design.

\body

Introduction

The production of metallo-β-lactamases (MBLs) by Gram-negative pathogens such as *Escherichia coli*, *Klebsiella pneumoniae*, *Acinetobacter baumannii*, *Pseudomonas aeruginosa* and *Stenotrophomonas maltophilia* is a major contributor to bacterial antibiotic resistance (1, 2). MBLs are able to hydrolyze most β-lactam antibiotics, including clinically important serine β-lactamase inhibitors (βLIs, clavulanic acid and penicillanic acid sulfones) and the carbapenems, which are often used as a 'last-resort' therapy for serious infections (3-6). MBLs can be divided into three subclasses, B1, B2 and B3, based on sequence, structure and zinc ion utilization (2, 7-9). All three classes contain a similar overall αββα fold, with the active site lying in a groove between the two β-sheets (**Figure 1**). In most di-zinc B1 enzymes, such as IMP-1 (10), BcII (11) and NDM-1 (12), the Zn1 site is tetrahedrally coordinated by a water molecule (Wat1), H116, H118 and H196 (standard MBL numbering scheme (7) used throughout), while Zn2 is bound by Wat1, a second water molecule (Wat2), D120, C221 and H263 in a trigonal bipyrimidal coordination. A water molecule (Wat1) bridges/coordinates Zn1 and Zn2, in an arrangement that is suited to activate it as a nucleophile.

In mono-zinc B2 enzymes such as CphA (13) and Sfh-I (14), binding of the zinc ion is representative of the Zn2 site in B1 enzymes, with coordination by a water molecule (Wat1), D120, C221 and H263, in a tetrahedral rather than trigonal bipyrimidal geometry. Two water molecules (Wat1 and Wat2) are present in the active site, with Wat2 hydrogen-bonded to H118 and H196, and Wat1 coordinating Zn2, lying approximately equidistant between Zn2 (2.3 Å) and Wat2 (2.6 Å). Wat2 is believed to be activated by H118, rather than a zinc ion, to act as the nucleophile during antibiotic hydrolysis (14).

Di-zinc B3 enzymes (e.g. L1(15) and AIM-1(16)) have similar active-site architectures to B1 MBLs, with Zn1 in tetrahedral coordination with a water molecule (Wat1), H116, H118 and H196; and the nucleophilic water (Wat1) bridging Zn1 (1.9 Å) and Zn2 (2.1 Å). Zn2, however, is coordinated by D120, H121, H263 and an additional water molecule (Wat2) in a distorted trigonal bipyramidal geometry. To date clinically useful βLIs of any of the three MBL classes have not been identified, and the aforementioned structural differences have complicated development of βLIs with cross-class (B1, B2 and B3) activity.

In response to this urgent medical need, we have developed and synthesized four bisthiazolidine (BTZ) compounds, L-CS319 (**1a**), D-CS319 (**1b**), L-VC26 (**2a**) and D-VC26

(**2b**) (blue, gray, orange and cyan, respectively, **Figure 2**) (17, 18). These novel βLIs contain both a free thiol, which is a high affinity zinc-binding group, and two defining properties of β-lactam substrates, a feature hitherto overlooked in MBL inhibitor design. These are first a carboxylate moiety that in penicillins and carbapenems is able to bind Zn2 and interact with conserved residues on the protein main chain (19, 20); and, secondly, a tetrahedral bridgehead nitrogen that interacts with Zn2 as hydrolysis of bicyclic β-lactam antibiotics proceeds (21, 22). The absence of structural information on how a single compound can bind and inhibit all three classes of MBLs hinders further development of any potent cross-class inhibitors. We therefore characterized cross-class MBL inhibition *in vitro*, and in MBL producing bacteria, by the four previously synthesised BTZs, and obtained crystal structures for B1 (IMP-1 and BcII), B2 (Sfh-I) and B3 (L1) MBLs complexed with the novel scaffold, including one compound (**1a**) now structurally characterised in all three classes. These data demonstrate how a single compound class can utilize multiple modes of binding to inhibit, *in vitro* and in producer organisms, MBLs of different classes and active-site architectures; and identify routes to further improve potency against the range of target enzymes.

Results

BTZs are cross-class MBL inhibitors *in vitro*

Previous kinetic characterization of BTZ inhibition of selected MBL targets demonstrated them to be micromolar competitive inhibitors of carbapenem (imipenem) hydrolysis by the B1 MBLs VIM-2 and NDM-1, with K_is varying between 3.7 ± 0.3 and 19 ± 3 μM (17, 18) (**Table 1**). Here, we evaluate their cross-class inhibition potential by measuring the in vitro effect of BTZs on imipenem hydrolysis by other MBLs of the B1 [*Bacillus cereus* BcII (11, 23, 24) and *Serratia marsescens* IMP-1 (10)], B2 [*Serratia fonticola* Sfh-I (14, 25)] and B3 [*S. maltophilia* L1 (15, 26)]. To ensure coverage of diverse MBLs, we also assayed activity against the structurally-uncharacterized, atypical *Elizabethkingia meningoseptica* GOB-18, reconstituted in its fully active monozinc form (27).

These data reveal the compounds to be competitive, micromolar inhibitors of all MBL classes (**Figures S1 and S2**), with K_is between 0.26 ± 0.03 μM and 84 ± 6 μM (**Table 1**). The inhibition of B1 MBLs is little affected by the stereochemistry on the BTZs (D- (**1b**, **2b**) or L- (**1a**, **2a**) BTZs), or by the presence of a *gem*-dimethyl group (**2a**, **2b**), with K_i values varying by 2 and 2.5-fold (IMP-1 and BcII, respectively). In particular, BTZ potency against IMP-1 is the same for both enantiomers, while the addition of a *gem*-dimethyl group (**2a**/**2b**) resulted in a 2-fold increase in K_i. In contrast, against BcII, D-BTZs were 1.5 to 2.5-fold less potent than the L-BTZs, while the *gem*-dimethyl group had little effect on potency (**2a**/**2b** K_i is up to 1.5-fold greater than **1a**/**1b**). Against the B3 MBL L1 all compounds exhibit near identical K_i values, between 10 and 12 μM ± 1-2, while only **2b** exhibits similar potency against the B3 MBL GOB-18 (10 μM), with the three other BTZs 3 to 4-fold less potent (30-41 μM ± 1-4). The unusual GOB-18 active site, in which the Zn1 ligand H116 is replaced by Q, and only the Zn2 site is occupied in vitro (27), likely accounts for these small differences we observe in potency against B3 enzymes. While it is possible periplasmic GOB-18 is di-zinc, as GOB-1 (28), importantly these data show the BTZ scaffold inhibits MBLs with even highly atypical active-site architectures. Only against B2 Sfh-I is there strong stereochemical preference, with L-BTZs (**1a**, **2a**) greater than 100-fold more potent than their corresponding D-enantiomers (**1b**, **2b**). As is the case for the B1 and B3 enzymes, there is little change in BTZ potency on addition of a *gem*-dimethyl group, with **1a** and **2a** exhibiting similar, submicromolar K_i values (0.26 ± 0.03 μM and 0.36 ± 0.04 μM, respectively).

BTZs restore β-lactam efficacy towards MBL producing isolates

To assess the clinical potential of BTZs, time-kill assays were performed using *E. coli* cells expressing the B1 MBLs IMP-1 and BcII, B2 Sfh-I and the B3 enzyme GOB-18 (**Figure S3**). Additionally, a multi-drug resistant *S. maltophilia* clinical isolate producing both the B3 MBL L1 and the serine β-lactamase L2 was also studied (**Figure 3 and Figure S4**). The βLIs do not have any antimicrobial effect on their own, as differences could not be detected in viable cell number between cells exposed to BTZs and broth-only controls. Viable cell counts following exposure to sub-lethal concentrations of β-lactams (imipenem and ticarcillin-clavulanate for the *E. coli* and *S. maltophilia* isolates, respectively) in the presence of BTZs demonstrated that BTZs are able to inactivate the MBLs in clinically relevant strains, as evidenced by the significant reductions in bacterial count ($>10^3$). Potentiation of antibiotic activity against *S. maltophilia* is particularly significant as strains of this Gram-negative pathogen tend to be extensively multidrug resistant, particularly due to the expression of two distinct β-lactamases and several membrane-spanning multidrug efflux pumps (29).

Structure determination of BTZ complexes with B1, B2 and B3 MBLs

An understanding of how BTZs inhibit all three classes of MBL requires structural information for representative BTZ:MBL complexes to complement our previously obtained structures of **1a** bound to the B1 MBLs VIM-2 and NDM-1 (17, 18). We therefore crystallized the MBLs IMP-1 and BcII (subclass B1), Sfh-I (B2) and L1 (B3) and soaked the crystals in the four BTZs. Co-complex structures were solved for IMP-1 with **1b** (2.30 Å resolution) and **2a** (2.30 Å); BcII with **1b** (1.80 Å); Sfh-I with **1a** (1.3 Å) and L1 with **1a** (1.63 Å), **1b** (1.84 Å) and **2b** (1.80 Å) (**Table S1**). For B2 Sfh-I we were unable to obtain a co-complex with both BTZ stereoisomers, consistent with the *in vitro* observation that D-BTZs were at least 100-fold less potent Sfh-I inhibitors than L-BTZs. In all seven cases there was clear F_o-F_c density in the MBL active site into which the corresponding ligand could be modelled (**Figure S5**). Further ligand validation statistics (real-space R-value, local ligand density fit and real-space correlation coefficient) are presented in **Table S2**.

IMP-1 crystallized in the space group $P2_12_12_1$, with four molecules in the asymmetric unit (ASU), not previously described. Electron density consistent with bound **2a** was observed in three of the four subunits (average B-factor 1.8 times greater than the protein main chain), whereas **1b** could be confidently modelled in all four molecules of the ASU (B-factors 1.1

times above main chain). For comparison, we have also solved, to 1.98 Å resolution, the structure of uncomplexed di-zinc IMP-1, also in the space group $P2_12_12_1$ (see **Supplemental Information**). BcII crystallized in the previously described space group C2 (30), with one molecule in the ASU and one molecule of **1b** identified in the active site (B-factor 1.6 times above main chain). Sfh-I crystallized in space group $P2_1$ (14), with **1a** clearly defined in both monomers of the ASU (B-factors 1.2 times above protein main chain). L1 crystallised in space group $P6_422$ (15), with one molecule in the ASU, into which **1a**, **1b** and **2b** were modelled into clearly defined density (B-factors 2.1, 1.8 and 1.7 above main chain). Ligands were refined at full occupancy for all but L1:**1b** (ligand occupancy 0.76) and L1:**2b** (0.81).

A dual-mode of binding for L-BTZs to MBLs.

The IMP-1:**2a** (**Figure 4A**) and L1:**1a** (**Figure 4B**) structures reveal similar binding modes for L-BTZs to IMP-1 (B1) and L1 (B3) (**Figure 4C**). These also resemble the previously observed binding mode of **1a** to both VIM-2 (18) and NDM-1 (17) (**Figure S6).** In all these structures, the thiol of the BTZ mercaptomethyl group is positioned nearly equidistant between the two zinc ions (between 2.22 and 2.43 Å ± 0.14 and 0.23 Å; see Table S1 for coordinate errors and **Table S3** for detailed distances). BTZ-binding displaces the zinc-bridging nucleophilic water/hydroxide (Wat1) that is observed in the native MBL active site (**Figure S7**) with a concomitant small increase in the Zn1 - Zn2 distance of *c*. 0.3/0.4 Å (± 0.14/0.23 Å), compared to uncomplexed enzymes (**Table S3**). L-BTZ-binding is further stabilized by direct interaction of its carboxylate with structurally equivalent side chains that are implicated in substrate binding (19, 20, 31), K224 in IMP-1 and S223 in L1. **1a** also makes hydrophobic interactions with two residues on L1 (W38 and P226), and **2a** contacts two (W64 and V67) on the flexible L3 loop (32) positioned above the IMP-1 active site (gray side chains in **Figure 4A and B**). Despite these similarities, BTZ-binding results in a larger ligand:protein buried surface area in the IMP-1:**2a** (330 $Å^2$) complex compared to L1:**1a** (264 $Å^2$), largely due to the L3 loop which is present in IMP-1 but not L1 (**Figure 4**).

In contrast, L-BTZ-binding to the mono-zinc B2 MBL Sfh-I differs substantially from that to B1 or B3 enzymes. In the complex with **1a**, the **1a**-carboxylate group interacts with the active-site zinc (1.84 ± 0.03 Å), and is within hydrogen-bonding distance of two protein side chains, N233 (2.97 ± 0.03 Å) and H196 (2.96 ± 0.03 Å) (**Figure 5A**). Binding to Sfh-I results in *c*. 265 $Å^2$ of buried surface area, and is stabilized by interactions with four hydrophobic

residues (W87, F156, I153, F236, gray, **Figure 5A**). In addition, although BTZ-binding has little effect on the overall Sfh-I structure [RMSD 0.33 Å over 228 Cα atoms, compared to native Sfh-I (14)] there are significant rearrangements within the active site (**Figure 5B**). The BTZ-carboxylate displaces the water zinc ligand (Wat1), maintaining the tetrahedral zinc geometry, and causing a flip and *c*. 0.6 Å (± 0.03 Å) movement of the H196 side chain. This movement results in a loss of interaction of H196-Nε2 with the nucleophilic water (Wat2), which moves 0.9 Å deeper into the active site and closer to Zn2 (3.0 Å compared to 3.5 Å in uncomplexed Sfh-I, ± 0.03 Å). Notably, and in direct contrast to the structures obtained for complexes with IMP-1 and L1, the BTZ thiol is not involved in interactions with the Sfh-I zinc site.

A distinct mode of D-BTZ binding to L1

We next investigated binding of D-BTZ inhibitors to our chosen MBL targets. Surprisingly, structural analysis of D-BTZs bound to the B3 enzyme L1 revealed a third mode of binding. Similar to the L1:**1a** complex, the **1b**-mercaptomethyl group dominates L1 active-site interactions, with the thiol bridging the two zinc ions, again resulting in a small (0.4 ± 0.17 Å) increase in the Zn1-Zn2 distance (**Table S3**). However, the carboxylate group is no longer bound to S223, but instead interacts, via a water molecule, with Y32 on the non-conserved N-terminal extension of L1 (2.74 Å BTZ - water, 2.40 Å water - Y32, ± 0.17 Å, **Figure 6A**). This interaction causes an approximate 90° rotation of D-BTZ around the thiol compared to L-BTZ, orientating the BTZ to make hydrophobic interactions with three residues (P226, F156, I162, **Figure 6B**) of which only P226 is involved in binding **1a**. Despite this, the buried surface area on ligand binding is similar in both the L1:**1a** and L1:**1b** complexes (264 $Å^2$ and 268 $Å^2$, respectively). The structure of L1:**2b** indicates that the presence of a dimethyl group does not affect this mode of binding, although unsurprisingly there is a slight increase in the buried surface area (279 $Å^2$). **2b** makes the same hydrophobic interactions as **1b** (**Figure 6C**) and is bound with similar thiol-zinc and Zn1-Zn2 distances (**Table S3**). As in the L1:**1b** structure, interaction of the **2b** carboxylate with Y32 is also mediated by a water molecule (2.81 Å **2b** - water, 2.53 Å water - Y32, ± 0.18 Å).

1b binding to B1 MBLs involves multiple ligand-zinc interactions

Structures of **1b** bound to the B1 enzymes BcII and IMP-1 reveal multiple interactions of the inhibitor with both zinc ions in the active site (**Figure 7**). However, BTZ binding does not result in global conformational changes for either IMP-1 (IMP:**1b** compared to uncomplexed IMP-1 RMSD=0.28 Å over 222 Cα atoms) or BcII (BcII:**1b** compared to uncomplexed BcII RMSD=0.41 Å over 223 Cα atoms). **1b** binding to IMP-1 (buried surface area 292 $Å^2$) features four ligand-zinc interactions (**Figure 7A**), the carboxylate (2.1 ± 0.26 Å) and bridging nitrogen (2.8 ± 0.26 Å) with Zn2, and the thiol bridging Zn1 (2.0 ± 0.26 Å) and Zn2 (2.2 ± 0.26 Å), with the Zn1-Zn2 distance increasing by 0.2-0.3 Å (± 0.26 Å). Binding is further favored by interaction of the carboxylate with Lys224, as is the case with 2a binding to IMP-1.

As in the IMP-1:2a complex, residues W64 and V67 in the L3 loop are involved in hydrophobic interactions with the inhibitor, with W64 in particular forming π-stacking interactions with the BTZ bicyclic ring. Despite previous observations the NDM-1 L3 loop may 'close' on **1a** binding (17), the position of the IMP-1 L3 loop is more stable, with no substantial conformational shifts evident on BTZ-binding compared to the native structure. **1b** makes very similar interactions (**Figure 7B**) on binding BcII (buried surface area 287 $Å^2$), i.e., the carboxylate (2.0 ± 0.13 Å) and bridging nitrogen (2.7 ± 0.13 Å) with Zn2, the carboxylate with K224 (2.9 ± 0.13 Å), and the thiol equidistant between active-site zincs (2.2 ± 0.13 Å), with the Zn1 - Zn2 distance increasing by 0.3 ± 0.13 Å compared to uncomplexed BcII (PDB 4C09). Three hydrophobic interactions are formed, one with W87 and two with residues F61 and V67 in the L3 loop, which form after the L3 loop closes by approximately 3.0-4.6 ± 0.13 Å compared to its position in the native structure (**Figure S8**). As observed in the **1a**:Sfh-I complex, there are also important rearrangements within the IMP-1 and BcII active sites on **1b** binding (**Figure 7C and D**). Remarkably, the electron density clearly defines a displacement of the Zn2 ligand D120 and consequent loss of the D120-Zn2 coordination interaction (**Figure S9**). Instead, D120 reorients to form hydrogen bonds with either E59 (IMP-1) or S69 (BcII). This results in an irregular five-coordinate geometry for Zn2 and a 1.0 ± 0.26 Å (IMP-1) or 0.7 ± 0.13 Å (BcII) movement of Zn2 away from D120.

Discussion

Here we show the structural basis for micromolar competitive inhibition of all three MBL classes by BTZs, including of clinically relevant enzymes from opportunist bacterial pathogens, such as *E. coli*, *P. aeruginosa* or *S. maltophilia*, which can cause severe or even life-threatening infections. BTZs are able to cross the outer membrane of Gram-negative bacteria and enter the periplasm, inhibiting MBL activity *in vivo* and potentiating the activity of carbapenems and other β-lactams against MBL-producing clinical isolates. Our data demonstrate this simple scaffold, which in several aspects resembles the architecture of the bicyclic β-lactam substrate, is able to overcome the variations in MBL active-site architecture across subclasses to achieve roughly equipotent inhibition of all MBLs tested. Such variations, which encompass differences in zinc ligands, interaction partners for the carboxylate group at C2/C3 of β-lactams and the positions and locations of hydrophobic surfaces and conformationally flexible surface loops adjacent to the active site, have manifest as substantial differences in potency against different MBL targets for some other inhibitor classes. Unexpectedly our structural data reveal that BTZ inhibition of different MBLs is unique and characterised by multiple binding modes that vary both with target enzyme and with the BTZ enantiomer used.

The crystal structures of MBL:BTZ complexes presented here and in previous publications (17, 18) identify that BTZs utilize *four* distinct modes of binding to the range of MBL targets. L-BTZs adopt similar binding modes to the B1 and B3 binuclear enzymes, with overall BTZ orientation retained across enzymes that utilize different side chains [K224 (BcII, IMP-1, NDM-1); R228 (VIM-2) and S223 (L1)] in interactions with the BTZ carboxylate group that may or may not involve the intermediacy of (a) bound water molecule(s). This binding mode is also robust to differences in the composition (particularly with respect to the positions of aromatic residues) and orientation of the mobile L3 loop that is a feature of most B1 MBLs, but absent in B3 enzymes such as L1.

In contrast, D-BTZ binding differs profoundly between complex structures for B1 (BcII, IMP-1) and B3 (L1) enzymes, with interactions involving the carboxylate group (with Zn2 and the K224 side chain) a feature of the BcII and IMP-1 complexes but absent from those with L1. The differing L1 active-site architecture, which compared to B1 MBLs lacks an extended L3 loop and instead features elongated linkers between other secondary structural elements adjacent to the active site and hydrophobic residues at different positions, likely

imposes a different orientation upon the bound D-BTZ ligand. The fourth binding mode is observed in B2 MBL Sfh-I complexed with **1a**. In B2 enzymes conserved hydrophobic residues on the long α3 helix adjacent to the active site form a 'hydrophobic wall' proposed to contribute to selective carbapenem binding (33, 34). In the Sfh-I:**1b** structure, the BTZ thiol was observed buried deep into the hydrophobic cavity formed by residues W87, I153, F236 and F156, rather than, as anticipated, involved in interactions with the zinc center. We consider it likely that positioning of the thiol moiety in this cavity by the unique 'hydrophobic wall' of B2 MBLs also explains the high selectivity of Sfh-I for L- over D-BTZs, which is not observed in the B1 and B3 family members studied in this work. In addition, the carboxylate of bound D-BTZ would be positioned differently at the Zn site, requiring different ancillary interactions with the protein main chain. In Sfh-I, unlike our observations of BTZ-binding to L1 and IMP-1, the more constrained active site provides little room for a second BTZ binding mode. It is likely that significant conformational changes within the active site would be required to bind D-BTZs, resulting in higher K_i's *in vitro*, while in the crystalline state these are prevented by packing interactions. Taken together, these data clearly indicate that the variation in active-site architecture between different MBLs is such that the ability to support more than one mode of binding may be necessary to achieve activity towards the full range of targets for even simple inhibitor scaffolds.

Investigation of the activity of BTZs as potential MBL inhibitors was in part prompted by their structural similarities to β-lactam substrates. Comparison of L-BTZ:MBL and hydrolyzed substrate:MBL structures highlights both differences and similarities in the mode(s) of ligand binding (**Figure 8**). B1 and B3 MBLs bind antibiotic similarly, exemplified by the NDM-1:ampicillin (19) (green, **Figure 8A**) and L1:moxalactam (20) (green, **Figure 8B**) structures, respectively. In particular, in binuclear MBLs K224 (B1) or S223 (B3) interact with the carboxylate at C2/C3 of the hydrolyzed β-lactam. However, in both cases β-lactam binding is also characterised by interactions of Zn2 with the β-lactam nitrogen and carboxylate, whereas equivalent interactions are not observed in the **1a**:MBL complexes. The absence of an interaction between the BTZ-nitrogen (a component of the bicyclic ring structure) and Zn2 is however consistent with several models of MBL-catalyzed antibiotic hydrolysis that feature Zn2-coordination by the β-lactam nitrogen only after the amide bond has been cleaved and the β-lactam ring opened (21, 22). On the other hand, BTZ binding involves the thiol group bridging Zn1 and Zn2, and displacement of the nucleophilic water (Wat1), while in complexes with hydrolyzed antibiotics Wat1 is present (19, 20), albeit with differences in zinc geometry.

These differences are particularly evident in the NDM-1:ampicillin structure [PDB 3Q6X (19)] where Wat1 is more tightly bound to a trigonal byprimidal Zn1 (2.1 Å) than Zn2 (2.7 A). In comparison, in the native NDM-1 structure [PDB 3SPU (12)] Wat1 is more consistently (between the five chains in the ASU) equidistant between Zn1 (tetrahedral geometry) and Zn2. **1b** binding to L1 also involves fewer interactions with Zn2 than hydrolyzed antibiotic (**Figure 8C**), although it is notable that Y32, which helps to stabilize inhibitor binding by interaction with the BTZ-carboxylate, also stabilises antibiotic binding through interaction with the moxalactam carbonyl oxygen (20).

In comparison to MBL:L-BTZ complexes, (or binding of D-BTZs to L1), **1b** binding to the B1 MBLs IMP-1 and BcII more closely represents that of hydrolyzed β-lactams. This is most evident with respect to interactions involving Zn2 and Lys224, as highlighted by comparison of IMP-1:**1b** and BcII:**1b** complexes with that of hydrolyzed ampicillin bound to NDM-1 (19) (**Figure 9A and B,** respectively). In particular, both the BTZ and ampicillin carboxylate groups interact with Zn2 (2.0-2.2 Å) and hydrogen bond to Lys224 Nε (2.5-2.9Å). Furthermore, the bridgehead nitrogen of D-BTZs lies within coordination distance of Zn2 (2.7-2.8 ± 0.13/0.26 Å), although this interaction is not as strong as the equivalent in the NDM-1:ampicillin complex involving the β-lactam nitrogen (2.2 Å) (**Figure 9C-E**). However, despite the closer resemblance of their binding to that of antibiotic substrates, comparison of K_i values shows D-BTZs to be no more effective B1 MBL inhibitors than the L-BTZs that exhibit different binding modes (see **Table 1**). This may arise from D-BTZ-binding causing the energetically unfavourable disruption of the D120-Zn2 interaction. This D120 rearrangement may be necessary to relieve conformational strain about the Zn2 site arising from interaction with bound D-BTZ, or may be a means of relieving steric clashes due to the orientation of D-BTZ in the active site imposed by interactions involving the carboxylate group and, in particular, positioning of the sulphur atom as a bridging ligand to both zinc ions.

Similar to B1 and B3 enzymes, structural characterisation of hydrolyzed biapenem binding to the B2 MBL CphA (34) (green, **Figure 8D**) reveals the antibiotic to interact with Zn2 via its β-lactam nitrogen atom and carboxylate group, and by hydrogen bonds to Lys224, Thr157 and T119. In comparison, in Sfh-I:**1a**, the BTZ carboxylate group, and not the nitrogen atom, interacts with the Sfh-I zinc ion, as well as two residues that are not involved in antibiotic binding to CphA, H196 and N233 (blue, **Figure 8D**). Binding of hydrolyzed biapenem also involves residues W87, I153, F236 and F156 of the 'hydrophobic wall', a unique structural feature of B2 MBLs. These residues also stabilize binding of **1a**, specifically the thiol moiety,

indicating that the 'hydrophobic wall' is also important in BTZ binding by B2 MBLs (34). However, while thiol compounds have been shown as high affinity MBL ligands (35), giving rise to the identification of a variety of thiol-based inhibitors, the absence of thiol:Zn2 interactions in our Sfh-I:BTZ crystal structure supports consideration of other metal binding groups, such as carboxylates or phosphonates, in searches for broad-spectrum MBL inhibitors.

Numerous chemical scaffolds have been explored as candidate MBL inhibitors, in a search that is given added impetus by the increasing dissemination of MBLs on mobile genetic elements and in clinically significant pathogens. However, studies to date have focussed upon relatively restricted numbers of target enzymes, and characterization, particularly at structural level, has not in most cases extended to all three enzyme subclasses. Captopril (an angiotensin-converting enzyme and MBL inhibitor) is the most studied MBL inhibitor, with complexes of one or both of its enantiomers described for B1 [BcII (PDB 4C1H (36) and 4C1C (36)), BlaB (37), IMP-1 (PDB 4C1G and 4C1F (36)), NDM-1 (38) and VIM-2 (PDB 4C1D and 4C1E (36))], B2 [CphA (35)] and B3 [L1 (39)] MBLs. Hence we compared the BTZ binding modes described here to those of L- and D-captopril, which, like BTZs, feature a carboxylate group attached to a ring system and a free thiol group, but lacks the bicyclic organization and bridgehead nitrogen of the BTZ scaffold. Similar to BTZ complexes, the free thiol of D- or L-captopril bridges the active-site zinc ions of both B1 (IMP-1 and BcII) and B3 (L1) MBLs (**Figure S10A-E**), while the carboxylate interacts with K224 (B1), S223 (B3), or R228 (B1 VIM-2). However, D-captopril binding to L1 does not involve Y32, as in the L1:**1b** structure (**Figure S10D**), and unlike **1b** binding to BcII and IMP-1 (**Figure S10B and S10C**), D-captopril binding to these targets does not feature Zn2-nitrogen or Zn2-carboxylate interactions.

Some other thiol-based inhibitors, such as the thioenolate ML302F (30), or mercaptoacetic acids (40), have been noted to make additional interactions with Zn2 through their carboxylate groups. Resemblance of D-captopril and BTZ binding is most apparent for the B2 enzymes, where D-captopril binds to the active site of CphA through interaction of its carboxylate group with the zinc ion (35), as observed in the Sfh-I:**1a** structure (**Figure S10F**). However, thiol-binding to the Zn2 site of B2 enzymes is possible, as observed previously in a CphA:inhibitor co-crystal structure (PDB 3IOF) (41). These data may indicate that, when both a thiol and carboxylate are present, the carboxylate-Zn2 interaction may be preferable, possibly as a result of the ability of the carboxylate group to make ancillary interactions with the protein main chain.

A major hurdle in the development of small molecules as effective countermeasures for infections by opportunistic Gram-negative bacteria is the requirement to penetrate the outer envelope of the bacterial cell. Many Enterobacteriaceae, and in addition non-fermenting species such as *A. baumannii* or *P. aeruginosa*, have limited permeability towards many small molecule solutes. In a previous investigation we established that BTZs can penetrate Gram-negative bacteria that express the NDM-1 MBL (17). The present work extends these results significantly by demonstrating BTZ inhibition (as evidenced by potentiation of carbapenem antimicrobial activity) of MBL activity for enzymes of all three subclasses expressed in *E. coli*. However, to investigate the ability of BTZs to penetrate more challenging organisms, we also assessed MBL inhibition in clinical *S. maltophilia* isolates. *S. maltophilia* is a versatile opportunist pathogen of compromised patients (42), and is attracting increasing attention as a pathogen of note in the biology of cystic fibrosis lung disease, with chronic infection identified as a risk factor for pulmonary exacerbations (43). *S. maltophilia* is a notoriously resistant organism with increased efflux pump activity, porin reduction, and two inducible β-lactamases (L1 and L2), that collectively confer resistance to most β-lactams (29). Ticarcillin-clavulanate is a combination shown to be effective against some *S. maltophilia* infections (44), but may be compromised by β-lactamase production (45). Therefore, the ability of BTZs to restore β-lactam efficacy against a nosocomial *S. maltophilia* isolate indicates potential effectiveness in clinically relevant situations, where cross-class inhibition must extend to extensively drug-resistant physiological strains.

In closing, we report BTZs achieve cross-class MBL inhibition despite the structural diversity and zinc requirements of the different enzyme targets. The ability of the unique BTZ scaffold to bind in multiple orientations is likely due to the substrate-like design that is decorated with two strong metal-binding groups (-SH and -COOH). Indeed, the multiple binding modes possible for B1 and B3 enzymes accord with the broad substrate spectrum of these enzymes, while the B2 MBL, which shows preference for carbapenem substrates, shows some stereochemical preference. BTZs therefore provide a novel, efficient strategy for cross-class MBL inhibition, show activity against target bacterial pathogens as well as *in vitro*, and thus justify efforts at further improvement to enhance potency and clinical applicability.

Materials and Methods

Synthesis of bisthiazolidines

1a (L-CS319; (2R,5S,8R)-8-carboxylate-2-mercaptomethyl-1-aza-3,6-dithiobicyclo[3.3.0] octane); **1b** (D-CS319; (2S,5R,8S)-8-carboxylate-2-mercaptomethyl-1-aza-3,6-dithiobicyclo[3.3.0] octane); **2a** (L-VC26; (2R,5S,8R)-2-mercaptomethyl-7-dimethyl-8-carboxylate-1-aza-3,6-dithiobicyclo[3.3.0] octane); and **2b** (D-VC26; (2S,5R,8S)-2-mercaptomethyl-7-dimethyl-8-carboxylate-1-aza-3,6-dithiobicyclo[3.3.0] octane) were synthesised as previously described (18). The L- and D- notation thus refers to the 2R,5S,8R and 2S,5R,8S chiralities of the BTZs, respectively.

Purification of soluble MBLs.

IMP-1, L1 and Sfh-I lacking the first 21 amino acids were cloned into pOPINF vectors (46) resulting in N-terminally His_6-tagged protein cleavable with 3C protease. BcII was cloned into the pET28a vector (Novagen) using NdeI and SalI restriction sites, resulting in N-terminally His_6-tagged protein cleavable with thrombin. For IMP-1, L1 and Sfh-I production, *E. coli* SoluBL21 (DE3) cells (Genlantis) bearing pOPINF were grown at 37 °C in auto-induction terrific broth media (Formedium) for 8 h then left overnight at 20 °C. BcII was overexpressed in *E. coli* BL21(DE3), grown at 37 °C in LB medium to A_{600} 0.6, when 0.5 mM IPTG and 0.5 mM $ZnSO_4$ were added (16 h, 18 °C). Cells were harvested by centrifugation (6,500 xg, 10 min).

For L1, cells were resuspended in 50 mM HEPES pH 8.0, 400 mM NaCl, Complete EDTA-free protease inhibitor mixture (Roche), 10 µM $ZnCl_2$ and broken by two passages through a cell disruptor (30,000 psi). After centrifugation (100,000 x *g*, 1h), supernatant (plus 8 mM imidazole) was incubated 2 hrs with Ni-NTA resin (Qiagen). 1 mM β-mercaptoethanol was included in all subsequent buffers. Protein bound resin was washed in Buffer A (50 mM Tris pH 7.5, 400 mM NaCl, 10 µM $ZnCl_2$) plus 10 mM imidazole, then with the same buffer plus 0.1% Triton X-100. Resin was further washed in Buffer A plus 20 mM imidazole and protein eluted in 50 mM Tris pH 7.5, 200 mM NaCl, 10 µM $ZnCl_2$, 400 mM imidazole. Imidazole was reduced to 10 mM in an Amicon 10 kDa molecular weight cut-off (mwco) concentrator. The tag was removed by 3C protease cleavage (4 °C, overnight) and capture on Ni-NTA resin. L1 was subsequently loaded onto a Superdex S200 column equilibrated in 10 mM Tris pH 7.0, 100 mM NaCl, 100 µM $ZnS0_4$. Peak fractions were concentrated to 23 mg/ml. For crystallisation, L1 protein was supplemented with 5 mM $ZnSO_4$. IMP-1 was purified

similar to L1, except 1 mM TCEP (rather than β-mercaptoethanol) was included in all buffers, and protein loaded onto a Superdex S75 column equilibrated in 50 mM Tris pH 7.5, 150 mM NaCl, 100 μM $ZnCl_2$, 1 mM TCEP and concentrated to 25 mg/ml. Sfh-I was purified as L1, except protein was loaded on to a Superdex S75 column equilibrated in 50 mM HEPES pH 7.0 and concentrated to 15 mg/ml. For BcII, cells were re-suspended in Buffer B (50 mM Tris pH 8.0, 200 mM NaCl) supplemented with 10 μg/mL DNAse, 4 mM $MgCl_2$, and 2 mM phenylmethylsulfonyl fluoride (PMSF) and disrupted by sonication. After centrifugation (60 min, 15,000 g) and supernatant loaded on to Ni-sepharose resin equilibrated with Buffer A. The column was washed with 100 mL of Buffer B and BcII was eluted with Buffer B plus 500 mM imidazole using a linear gradient (0-100% Buffer B, over 100 ml). The his-tag was removed with thrombin and capture on Ni-sepharose resin. Flow-through (cleaved BcII) was diluted (1:5) in Buffer C (100 mM HEPES pH 7.0, 1 mM $ZnSO_4$) and loaded on to CM-sepharose resin equilibrated with Buffer C. The column was washed with 100 mL of Buffer C and BcII was eluted with Buffer C plus 400 mM NaCl, with a purity > 95%, as determined by SDS-PAGE. Protein was concentrated to 15 mg/ml using Centricon ultrafiltration devices (Millipore, Bedford, MA, USA) and exchanged into 10 mM Tris-HCl pH 7, 50 mM NaCl, 1 mM DTT, and 1 mM $ZnSO_4$.

GOB-18 was purified cytoplasmically, and reconstituted in its fully active monozinc form, as previously described (27).

Enzyme assays

Inhibition constants (K_i) were determined by following imipenem hydrolysis at 300 nm absorbance (JascoV-670 spectrophotometer) in Buffer C (10 mM HEPES pH 7.5, 0.2 M NaCl, 50 μg/mL BSA; B1 and B3 enzymes) or Buffer C plus 20 μM $ZnSO_4$ (B2 Sfh-I). BTZs were dissolved in DMSO (30 mM) and diluted in reaction buffer to the desired concentration. The presence of 1% DMSO did not alter the enzyme activity. Assays were initiated by enzyme addition to the substrate and inhibitor mixture. K_i's were determined by data fitting to the Competitive Inhibition Model implemented in GraphPad Prism 5.0.

In vitro time-kill study.

Escherichia coli DH5α carrying the pMBLe plasmid (17) expressing MBLs BcII, IMP-1, Sfh-I and GOB-18 were cultured overnight at 37 ºC in Mueller Hinton Broth (MHB) supplemented with 25 mg/L gentamycin. 1.5 µl of the overnight cultures were inoculated in 1 mL MHB supplemented with 100 µM IPTG to obtain a bacterial suspension of approximately 10^6 CFU/mL. To examine the effects of the novel BTZs compounds on bacterial growth, bacterial suspensions were grown at 37 ºC under different conditions: MHB alone (growth control), or supplemented with 0.4% DMSO (growth control), sub-lethal imipenem concentrations, 100 mg/L of each inhibitor, or a combination of imipenem and inhibitor. Samples (10 µl) were removed at intervals of 100, 300 and 500 min of exposure, and serial dilutions performed on MHB. Viable cell numbers were determined by spotting 20 µl of each dilution on Muller Hinton Agar (MHA). Plates were incubated (37 ºC overnight), and colonies counted. Results are the mean of three biological replicates. Assays using a clinical isolate of *S. maltophilia* (strain C1: L1 and L2 producer) were performed similarly except samples were taken after 4, 8 and 12 hours of treatment.

Crystallization and structure Determination.

L1 and Sfh-I were crystallized as previously described (14, 15). IMP-1 was crystallized using sitting drop vapor diffusion in CrysChem24 well plates (Hampton Research) at 18 °C. Drops were formed by mixing 1 µl protein solution with 1 µl crystallization reagent (0.1 M sodium cacodylate pH 6.0, 0.2 M sodium acetate, 25% PEG8000) and equilibrated against 500 µl. Crystals grew to maximum size in seven days. BcII was crystallized using hanging-drop vapour diffusion in 24-well plates (Hampton Research) at 20 °C. Drops were formed by mixing 1 µl protein solution with 1 µl crystallization reagent (180 mM K_2SO_4, 20 % PEG 3350, 1 mM DTT, and 1 mM $ZnSO_4$) and equilibrated against 1 ml. Crystals grew to maximum size within 3–5 days.

Inhibitor bound complexes were obtained by soaking crystals for 15–60 min in 2-5 mM inhibitor dissolved in cryoprotectant [L1: 0.05 M HEPES pH 7.5, 1.75 M $(NH_4)_2SO_4$, 1.25% PEG400, 25% glycerol, 2 mM TCEP; IMP-1: 0.1 M sodium cacodylate, 0.15 M sodium acetate, 25% ethylene glycol, 15% PEG8000, 2 mM TCEP, 50 µM $ZnCl_2$; Sfh-I: 0.02 M HEPES pH7.5, 0.12 M sodium acetate, 14% PEG3350, 20% glycerol, 2 mM TCEP; BcII: reservoir plus 20% glycerol]. IMP-1 native crystals were cryoprotected by soaking (1 min) in IMP-1 cryoprotectant. Crystals were looped and flash-frozen in liquid nitrogen. Diffraction

data were collected at 100K on beamlines I02, I03, I04, I04-1 or I24 (Diamond Light Source, UK) or on a high-flux Rigaku RAXIS IV++ in-house X-ray generator (BcII, Los Alamos National Laboratory). Data sets were indexed and integrated using XDS (47), iMosflm (48) or HKL2000 (49) and scaled using Aimless in CCP4 (50) or HKL2000 (49). Crystals were not prone to radiation damage in all cases and relatively high R_{merge} values, compared to high I/σI values, are due to the high redundancy of the data, or in the case of BcII:**1b** due to the collection of data on a home source. Structures were phased by molecular replacement with Phaser (51) using as starting models PDB 3I13 (52) (BcII), 1SML (15) (L1), 1DD6 (10) (IMP-1) or 3SD9 (14) (Sfh-I). Structures were completed by iterative rounds of manual model building in Coot (53) and refinement in Phenix (54) or Refmac5 (55). Sfh-I crystals were pseudo-merohedrally twinned [twin law h,-k,-l, determined by Xtriage (54)], so the Sfh-I model was completed with twin refinement in Refmac5. Omit maps were calculated from the final model after removal of the ligand and refinement in Phenix (L1, IMP-1, BcII) or Refmac (Sfh-I). Ligand structures and geometric restraints were calculated with PRODRG (56) or Phenix eLBOW (57). Structure validation was assisted by Molprobity (58), SFCHECK (59), and Phenix. Figures were prepared using PyMol (60). Root mean square deviations (RMSDs) were calculated over Cα atoms aligned using PDBeFold (61). Ligand buried surface areas were calculated using PDBePisa (62).

Acknowledgments

We thank Diamond Light Source for beamtime (proposal MX313) and the staff of beamlines I02, I03, I04 and I04-1 and I24 for their help. The work was supported by a grant from the National Institute of Allergy and Infectious Diseases of the U.S. National Institutes of Health (R01AI100560 to L.I.L., G.M., R.B., A.J.V. and J.S; and in part R01AI063517 and R01AI072219 to R.A.B). The content is solely the responsibility of the authors and does not necessarily represent the official views of the National Institutes of Health. This study was supported in part by funds and/or facilities provided by the Cleveland Department of Veterans Affairs, Award Number 1I01BX001974 to R.A.B. from the Biomedical Laboratory Research & Development Service of the VA Office of Research and Development and the Geriatric Research Education and Clinical Center VISN 10 to R.A.B. J.S. acknowledges support from the U.K. Medical Research Council (U.K.-Canada Team Grant G1100135).

References

1. Walsh TR (2010) Emerging carbapenemases: a global perspective. *International journal of antimicrobial agents* 36 Suppl 3:S8-14.
2. Bush K & Jacoby GA (2010) Updated functional classification of beta-lactamases. *Antimicrobial agents and chemotherapy* 54(3):969-976.
3. Karsisiotis AI, Damblon CF, & Roberts GC (2014) A variety of roles for versatile zinc in metallo-beta-lactamases. *Metallomics : integrated biometal science* 6(7):1181-1197.
4. Bush K (2010) Alarming beta-lactamase-mediated resistance in multidrug-resistant Enterobacteriaceae. *Current opinion in microbiology* 13(5):558-564.
5. Fisher JF, Meroueh SO, & Mobashery S (2005) Bacterial resistance to beta-lactam antibiotics: compelling opportunism, compelling opportunity. *Chemical reviews* 105(2):395-424.
6. van Duin D, Kaye KS, Neuner EA, & Bonomo RA (2013) Carbapenem-resistant Enterobacteriaceae: a review of treatment and outcomes. *Diagnostic microbiology and infectious disease* 75(2):115-120.
7. Galleni M, *et al.* (2001) Standard numbering scheme for class B beta-lactamases. *Antimicrobial agents and chemotherapy* 45(3):660-663.
8. Bebrone C (2007) Metallo-beta-lactamases (classification, activity, genetic organization, structure, zinc coordination) and their superfamily. *Biochemical pharmacology* 74(12):1686-1701.
9. Palzkill T (2013) Metallo-beta-lactamase structure and function. *Annals of the New York Academy of Sciences* 1277:91-104.
10. Concha NO, *et al.* (2000) Crystal structure of the IMP-1 metallo beta-lactamase from Pseudomonas aeruginosa and its complex with a mercaptocarboxylate inhibitor: binding determinants of a potent, broad-spectrum inhibitor. *Biochemistry* 39(15):4288-4298.
11. Carfi A, Duee E, Galleni M, Frere JM, & Dideberg O (1998) 1.85 A resolution structure of the zinc (II) beta-lactamase from Bacillus cereus. *Acta crystallographica. Section D, Biological crystallography* 54(Pt 3):313-323.
12. King D & Strynadka N (2011) Crystal structure of New Delhi metallo-beta-lactamase reveals molecular basis for antibiotic resistance. *Protein science : a publication of the Protein Society* 20(9):1484-1491.

13. Bebrone C, *et al.* (2009) The structure of the dizinc subclass B2 metallo-beta-lactamase CphA reveals that the second inhibitory zinc ion binds in the histidine site. *Antimicrobial agents and chemotherapy* 53(10):4464-4471.
14. Fonseca F, Bromley EH, Saavedra MJ, Correia A, & Spencer J (2011) Crystal structure of Serratia fonticola Sfh-I: activation of the nucleophile in mono-zinc metallo-beta-lactamases. *Journal of molecular biology* 411(5):951-959.
15. Ullah JH, *et al.* (1998) The crystal structure of the L1 metallo-beta-lactamase from Stenotrophomonas maltophilia at 1.7 A resolution. *Journal of molecular biology* 284(1):125-136.
16. Leiros HK, *et al.* (2012) Crystal structure of the mobile metallo-beta-lactamase AIM-1 from Pseudomonas aeruginosa: insights into antibiotic binding and the role of Gln157. *Antimicrobial agents and chemotherapy* 56(8):4341-4353.
17. González MM, *et al.* (2015) Bisthiazolidines: A Substrate-Mimicking Scaffold as an Inhibitor of the NDM-1 Carbapenemase. *ACS Infectious Diseases*.
18. Mojica MF, *et al.* (2015) Exploring the Role of Residue 228 in Substrate and Inhibitor Recognition by VIM Metallo-beta-lactamases. *Biochemistry* 54(20):3183-3196.
19. Zhang H & Hao Q (2011) Crystal structure of NDM-1 reveals a common beta-lactam hydrolysis mechanism. *FASEB journal : official publication of the Federation of American Societies for Experimental Biology* 25(8):2574-2582.
20. Spencer J, *et al.* (2005) Antibiotic recognition by binuclear metallo-beta-lactamases revealed by X-ray crystallography. *Journal of the American Chemical Society* 127(41):14439-14444.
21. Tioni MF, *et al.* (2008) Trapping and characterization of a reaction intermediate in carbapenem hydrolysis by B. cereus metallo-beta-lactamase. *Journal of the American Chemical Society* 130(47):15852-15863.
22. Wang Z, Fast W, & Benkovic SJ (1999) On the mechanism of the metallo-beta-lactamase from Bacteroides fragilis. *Biochemistry* 38(31):10013-10023.
23. Rasia RM & Vila AJ (2002) Exploring the role and the binding affinity of a second zinc equivalent in B. cereus metallo-beta-lactamase. *Biochemistry* 41(6):1853-1860.
24. Felici A, *et al.* (1993) An overview of the kinetic parameters of class B beta-lactamases. *The Biochemical journal* 291 (Pt 1):151-155.
25. Fonseca F, *et al.* (2011) Biochemical characterization of Sfh-I, a subclass B2 metallo-beta-lactamase from Serratia fonticola UTAD54. *Antimicrobial agents and chemotherapy* 55(11):5392-5395.

26. Crowder MW, Walsh TR, Banovic L, Pettit M, & Spencer J (1998) Overexpression, purification, and characterization of the cloned metallo-beta-lactamase L1 from Stenotrophomonas maltophilia. *Antimicrobial agents and chemotherapy* 42(4):921-926.
27. Moran-Barrio J, *et al.* (2007) The metallo-beta-lactamase GOB is a mono-Zn(II) enzyme with a novel active site. *The Journal of biological chemistry* 282(25):18286-18293.
28. Horsfall LE, *et al.* (2011) Broad antibiotic resistance profile of the subclass B3 metallo-beta-lactamase GOB-1, a di-zinc enzyme. *The FEBS journal* 278(8):1252-1263.
29. Crossman LC, *et al.* (2008) The complete genome, comparative and functional analysis of Stenotrophomonas maltophilia reveals an organism heavily shielded by drug resistance determinants. *Genome Biol* 9(4):R74.
30. Brem J, *et al.* (2014) Rhodanine hydrolysis leads to potent thioenolate mediated metallo-beta-lactamase inhibition. *Nature chemistry* 6(12):1084-1090.
31. Feng H, *et al.* (2014) Structural and mechanistic insights into NDM-1 catalyzed hydrolysis of cephalosporins. *Journal of the American Chemical Society* 136(42):14694-14697.
32. Moali C, *et al.* (2003) Analysis of the importance of the metallo-beta-lactamase active site loop in substrate binding and catalysis. *Chemistry & biology* 10(4):319-329.
33. Brem J, *et al.* (2015) Studying the active-site loop movement of the Sao Paolo metallo-beta-lactamase-1. *Chemical science* 6(2):956-963.
34. Garau G, *et al.* (2005) A metallo-beta-lactamase enzyme in action: crystal structures of the monozinc carbapenemase CphA and its complex with biapenem. *Journal of molecular biology* 345(4):785-795.
35. Lienard BM, *et al.* (2008) Structural basis for the broad-spectrum inhibition of metallo-beta-lactamases by thiols. *Organic & biomolecular chemistry* 6(13):2282-2294.
36. Brem J, *et al.* (2015) Structural basis of metallo-beta-lactamase inhibition by captopril stereoisomers. *Antimicrobial agents and chemotherapy*.
37. Garcia-Saez I, *et al.* (2003) The 1.5-A structure of Chryseobacterium meningosepticum zinc beta-lactamase in complex with the inhibitor, D-captopril. *The Journal of biological chemistry* 278(26):23868-23873.

38. King DT, Worrall LJ, Gruninger R, & Strynadka NC (2012) New Delhi metallo-beta-lactamase: structural insights into beta-lactam recognition and inhibition. *Journal of the American Chemical Society* 134(28):11362-11365.
39. Nauton L, Kahn R, Garau G, Hernandez JF, & Dideberg O (2008) Structural insights into the design of inhibitors for the L1 metallo-beta-lactamase from Stenotrophomonas maltophilia. *Journal of molecular biology* 375(1):257-269.
40. Wachino J, *et al.* (2013) Structural insights into the subclass B3 metallo-beta-lactamase SMB-1 and the mode of inhibition by the common metallo-beta-lactamase inhibitor mercaptoacetate. *Antimicrobial agents and chemotherapy* 57(1):101-109.
41. Lassaux P, *et al.* (2010) Mercaptophosphonate compounds as broad-spectrum inhibitors of the metallo-beta-lactamases. *Journal of medicinal chemistry* 53(13):4862-4876.
42. Looney WJ, Narita M, & Muhlemann K (2009) Stenotrophomonas maltophilia: an emerging opportunist human pathogen. *Lancet Infect Dis* 9(5):312-323.
43. Waters V, *et al.* (2011) Stenotrophomonas maltophilia in cystic fibrosis: serologic response and effect on lung disease. *American journal of respiratory and critical care medicine* 183(5):635-640.
44. Falagas ME, Valkimadi PE, Huang YT, Matthaiou DK, & Hsueh PR (2008) Therapeutic options for Stenotrophomonas maltophilia infections beyond co-trimoxazole: a systematic review. *The Journal of antimicrobial chemotherapy* 62(5):889-894.
45. Chang YT, Lin CY, Chen YH, & Hsueh PR (2015) Update on infections caused by Stenotrophomonas maltophilia with particular attention to resistance mechanisms and therapeutic options. *Front Microbiol* 6:893.
46. Berrow NS, *et al.* (2007) A versatile ligation-independent cloning method suitable for high-throughput expression screening applications. *Nucleic acids research* 35(6):e45.
47. Kabsch W (2010) Xds. *Acta crystallographica. Section D, Biological crystallography* 66(Pt 2):125-132.
48. Battye TG, Kontogiannis L, Johnson O, Powell HR, & Leslie AG (2011) iMOSFLM: a new graphical interface for diffraction-image processing with MOSFLM. *Acta crystallographica. Section D, Biological crystallography* 67(Pt 4):271-281.
49. Otwinowski Z & Minor W (1997) Processing of X-ray diffraction data collected in oscillation mode. *Methods in Enzymology*, (Academic Press), Vol Volume 276, pp 307-326.

50. Winn MD, *et al.* (2011) Overview of the CCP4 suite and current developments. *Acta crystallographica. Section D, Biological crystallography* 67(Pt 4):235-242.
51. McCoy AJ, *et al.* (2007) Phaser crystallographic software. *Journal of applied crystallography* 40(Pt 4):658-674.
52. Gonzalez JM, Buschiazzo A, & Vila AJ (2010) Evidence of adaptability in metal coordination geometry and active-site loop conformation among B1 metallo-beta-lactamases. *Biochemistry* 49(36):7930-7938.
53. Emsley P & Cowtan K (2004) Coot: model-building tools for molecular graphics. *Acta crystallographica. Section D, Biological crystallography* 60(Pt 12 Pt 1):2126-2132.
54. Adams PD, *et al.* (2010) PHENIX: a comprehensive Python-based system for macromolecular structure solution. *Acta crystallographica. Section D, Biological crystallography* 66(Pt 2):213-221.
55. Murshudov GN, Vagin AA, & Dodson EJ (1997) Refinement of macromolecular structures by the maximum-likelihood method. *Acta crystallographica. Section D, Biological crystallography* 53(Pt 3):240-255.
56. Schuttelkopf AW & van Aalten DM (2004) PRODRG: a tool for high-throughput crystallography of protein-ligand complexes. *Acta crystallographica. Section D, Biological crystallography* 60(Pt 8):1355-1363.
57. Moriarty NW, Grosse-Kunstleve RW, & Adams PD (2009) electronic Ligand Builder and Optimization Workbench (eLBOW): a tool for ligand coordinate and restraint generation. *Acta crystallographica. Section D, Biological crystallography* 65(Pt 10):1074-1080.
58. Chen VB, *et al.* (2010) MolProbity: all-atom structure validation for macromolecular crystallography. *Acta crystallographica. Section D, Biological crystallography* 66(Pt 1):12-21.
59. Vaguine AA, Richelle J, & Wodak SJ (1999) SFCHECK: a unified set of procedures for evaluating the quality of macromolecular structure-factor data and their agreement with the atomic model. *Acta crystallographica. Section D, Biological crystallography* 55(Pt 1):191-205.
60. DeLano WL (2002) The PyMOL user's manual. *DeLano Scientific, San Carlos, CA* 452.

61. Krissinel E & Henrick K (2004) Secondary-structure matching (SSM), a new tool for fast protein structure alignment in three dimensions. *Acta crystallographica. Section D, Biological crystallography* 60(Pt 12 Pt 1):2256-2268.
62. Krissinel E & Henrick K (2007) Inference of macromolecular assemblies from crystalline state. *Journal of molecular biology* 372(3):774-797.

Figure Legends

Fig. 1. Architecture of B1, B2 and B3 metallo-β-lactamases.

The common αββα fold of representative MBLs is colored from N- (light blue) to C-terminus (light red), and is shown alongside a close up view of the active-site (boxed). Zinc ions (gray) and water molecules (red) are represented as spheres. Zinc coordination bonds are shown as gray dashes, with the corresponding residues (labelled) shown as sticks.
(A) B1 BcII (PDB 4C09)
(B) B2 Sfh-I (PDB 3SD9)
(C) B3 L1 (PDB 1SML)

Fig. 2. Chemical structures of bisthiazolidine inhibitors.

Bisthiazolidines **1a** (L-CS319, blue), **1b** (D-CS319, gray), **2a** (L-VC26, orange) and **2b** (D-VC26, cyan).

Fig. 3. Bisthiazolidines restore the in vitro activity of imipenem against a *Stenotrophomonas maltophilia* clinical isolate.

Bacteria were grown at sub-lethal concentrations of a mixture of ticarcillin (TIC, 64 µg/mL) and clavulanate (CLV, 2 µg/mL) or in combination with 100 µg/mL of each compound. Viable cells were recovered at 4, 8 and 12 hours. Results shown are the mean of three biological replicates +/- SD.

Fig. 4. L-bisthiazolidine binding to B1 (IMP-1) and B3 (L1) metallo-β-lactamases.

Close up view of IMP-1 and L1 active sites with bound L-BTZ (sticks, colored as Figure 2). Protein main chain is colored from N- (light blue) to C-terminus (light red). Residues which interact with the zinc ions (Zn1 and Zn2, gray spheres) are shown as sticks (colored as main chain), while hydrophobic residues that stabilize BTZ binding are shown as gray sticks. IMP-1 K224 and L1 S223 (labelled) interact with the BTZ carboxylate.
(A) 2a bound to B1 IMP-1. Protein-zinc interactions are shown as gray dashes and BTZ-protein or BTZ-zinc interactions are shown as yellow dashes.

(B) 1a bound to B3 L1. Interactions shown as in *A*.
(C) Superposition of IMP-1:**2a** (orange) and L1:**1a** (blue). BTZ-protein or BTZ-zinc interactions are shown as dashes colored orange (IMP-1:**2a**) or blue (L1:**1a**).

Fig. 5. 1a binding to Sfh-I and concomitant active-site conformational changes.

Active-site zinc ions (gray spheres) and water molecules (red spheres) are labelled.
(A) 1a (blue) bound in the active site of B2 Sfh-I (main chain colored as Figure 1). Hydrophobic residues, on the α3 region and within the active site, involved in binding **1a** are shown as gray sticks. The **1a** carboxylate bridges N233 and H196 (sticks). Residues involved in binding the active-site zinc ion (Zn2, gray sphere) and water (Wat2, red sphere) are represented as sticks. Interactions of **1a** with the protein main chain or Zn2 are shown as yellow dashes. Protein-zinc and protein-water interactions are shown as gray dashes.
(B) Superposition of Sfh-I:**1a** (blue) with unliganded, native Sfh-I (PDB 3SD9, green). Interactions of H118 and H196 with the BTZ or Wat2 are shown as dashes.

Fig. 6. 1b binding to B3 MBL L1.

A water molecule (red sphere) mediates the interaction of Y32 (sticks, labelled) with the D-BTZ carboxylate while S223 (sticks, labelled), which binds **1a**, is not involved. Hydrophobic and zinc-binding residues represented as Figure 4.
(A) 1b (gray) bound in the active site of B3 L1 (colored as Figure 4). Interactions shown as Figure 4.
(B) Superposition of L1:**1b** (gray) with L1:**1a** (blue). Interactions between the BTZ and protein are shown as gray or blue dashes, according to their respective structures.
(C) 2b (cyan) bound to B3 L1, represented as *B.*

Fig. 7. 1b binding to B1 MBLs BcII and IMP-1.

1b bound in the active of B1 MBLs **(A)** IMP-1 and **(B)** BcII (colors and interactions as Figure 4). In both *A* and *B,* K224 binds the **1b** carboxylate and the D120 – Zn2 coordination is disrupted. **(C)** Superposition of IMP-1:**1b** (gray; zinc ions light gray) with unliganded, native IMP-1 (green; zinc ions, dark gray). Binding causes movement of Zn2, and loss of the

D120 – Zn2 interaction.
(D) Superposition of BcII:**1b** (gray; zinc ions light gray) with unliganded, native BcII (PDB 4C09 green; zinc ions, dark gray). Binding is similar to *C*, causing the same rearrangements within the active site.

Fig. 8. Comparisons of the mode of binding between bisthizolidines and hydrolysed antibiotics.

Superpositions of **(A)** IMP-1:**1a** (orange; zinc ions, light gray) with NDM-1:hydrolyzed ampicillin (PDB 3Q6X, green; zinc ions, dark gray); **(B)** L1:**1a** (blue; zinc ions, light gray) with L1:moxalactam (PDB 2AIO, green; zinc ions, dark gray); **(C)** L1:**1b** (gray; zinc ions, light gray) with L1:moxalactam (as *B*); **(D)** Sfh-I:**1a** (gray; zinc ions, light gray) with CphA:biapenem (PDB 1X8I, green; zinc ions, dark gray).

Fig. 9. 1b binding to B1 MBLs IMP-1 and BcII closely resembles binding of hydrolysed antibiotic.

Superpositions of NDM-1:ampicillin (green) with **(A)** IMP:**1b** and **(B)** BcII:**1b** (gray; zinc ions, light gray). The modes of binding and ligand-protein/zinc interaction distances are shown in schematic representation for **(C)** NDM-1:hydrolysed ampicillin; **(D)** IMP-1:**1b** and **(E)** BcII:**1b**.

Figure 1

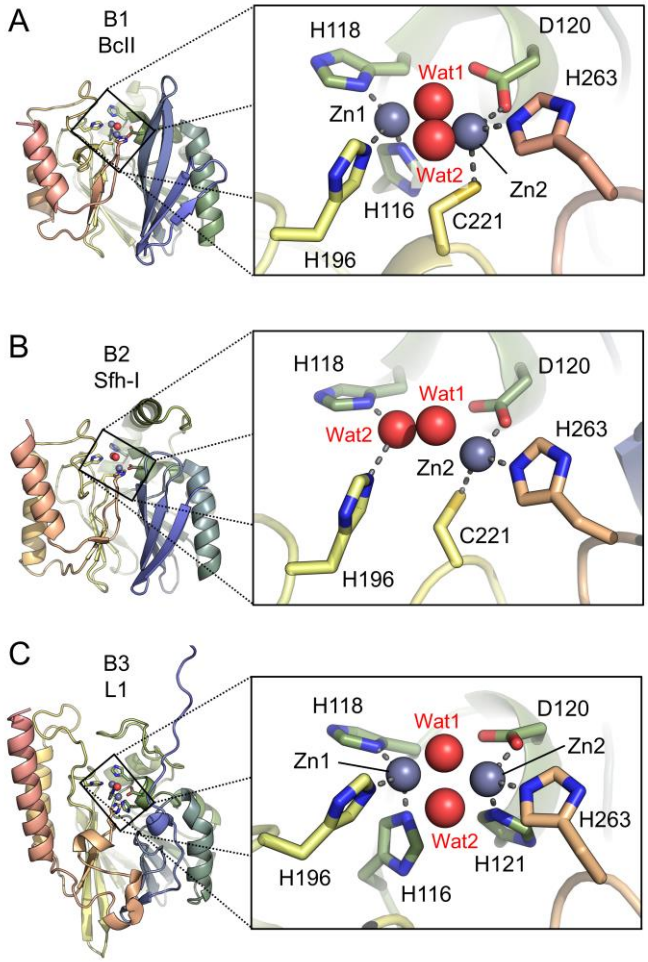
A
B1
BcII
H118
D120
Wat1
H263
Zn1
Wat2
Zn2
H116
C221
H196
B
B2
Sfh-I
H118
D120
Wat1
Wat2
H263
Zn2
C221
H196
C
B3
L1
H118
Wat1
D120
Zn1
Zn2
H263
Wat2
H121
H196
H116

Figure 2

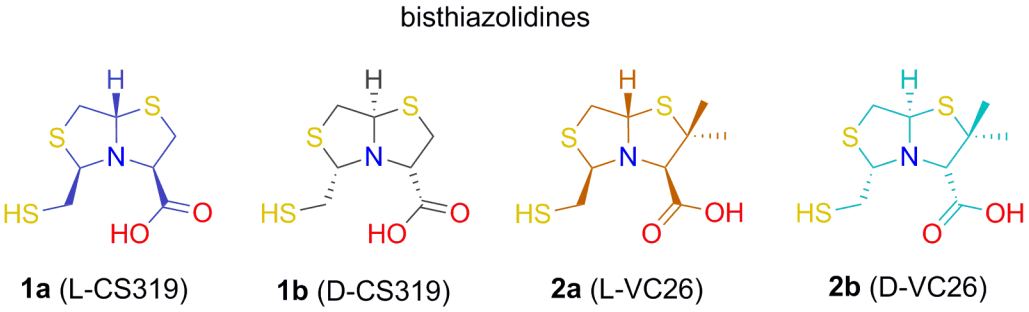
bisthiazolidines
H
S
S
N
HS
HO
O
1a (L-CS319)
1b (D-CS319)
OH
2a (L-VC26)
2b (D-VC26)

Figure 3

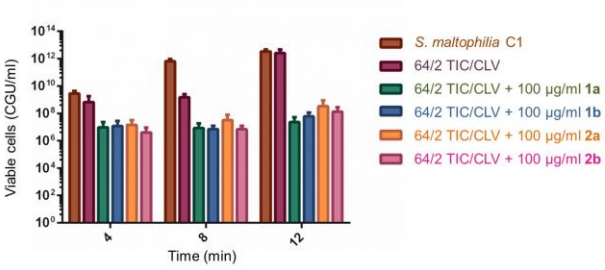
Viable cells (CGU/ml)
10^{14}
10^{12}
10^{10}
10^{8}
10^{6}
10^{4}
10^{2}
10^{0}
4
8
12
Time (min)
S. maltophilia C1
64/2 TIC/CLV
64/2 TIC/CLV + 100 µg/ml 1a
64/2 TIC/CLV + 100 µg/ml 1b
64/2 TIC/CLV + 100 µg/ml 2a
64/2 TIC/CLV + 100 µg/ml 2b

Figure 4

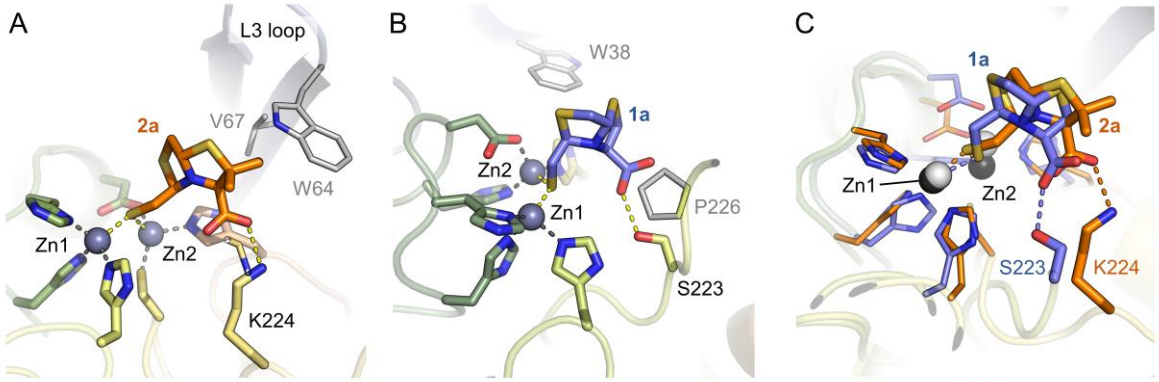

B1
IMP-1:**2a**

B3
L1:**1a**

IMP-1:**2a**
L1:**1a**

Figure 5

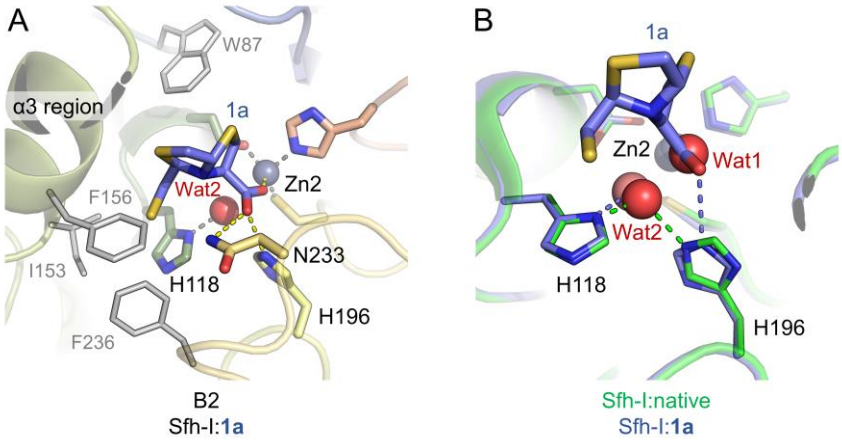
A
W87
α3 region
1a
Wat2
Zn2
F156
I153
N233
H118
H196
F236
B2
Sfh-I:1a
B
1a
Zn2
Wat1
Wat2
H118
H196
Sfh-I:native
Sfh-I:1a

Figure 6

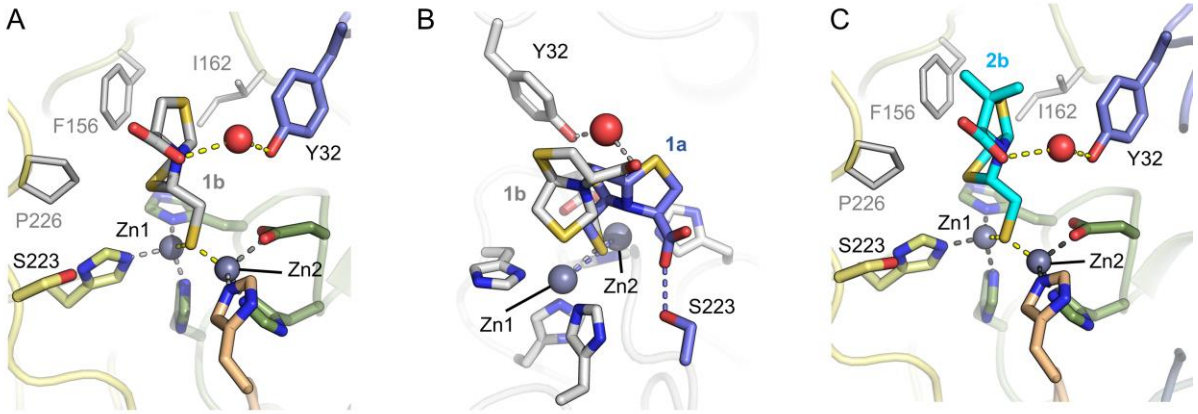

B3
L1:1b

L1:1b
L1:1a

B3
L1:2b

Figure 7

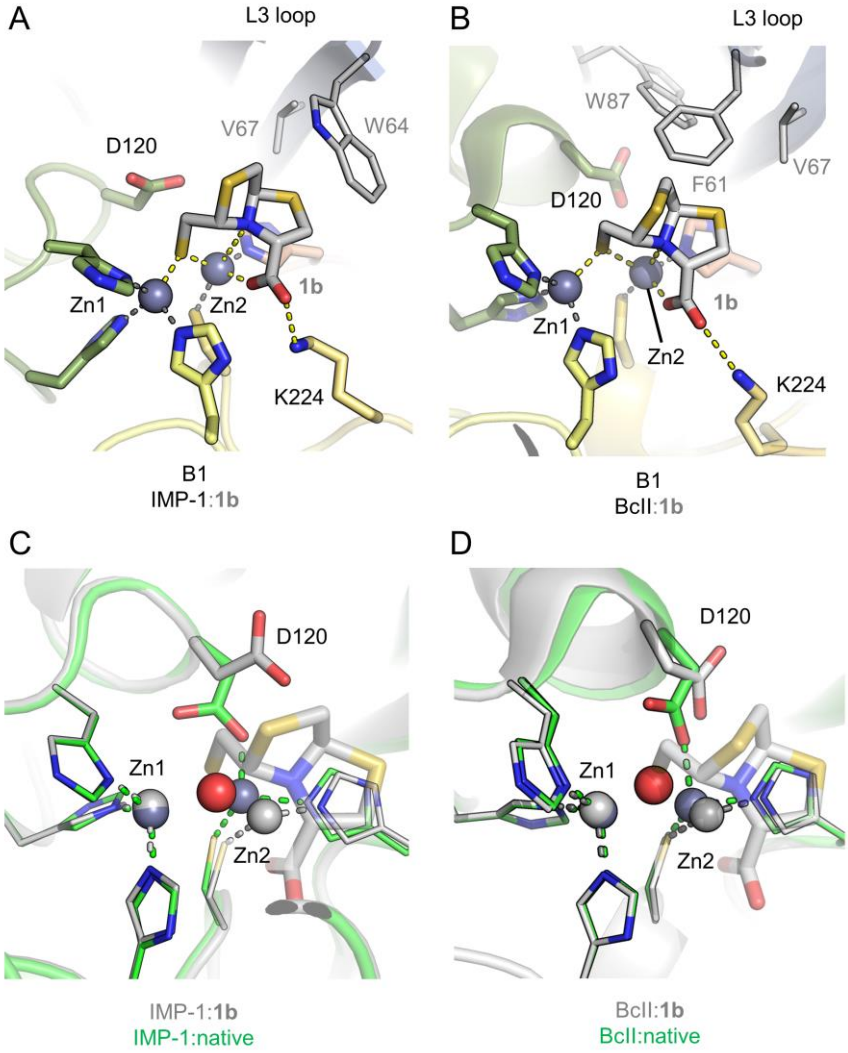
A
L3 loop
V67
W64
D120
Zn1
Zn2
1b
K224
B1
IMP-1:1b
B
L3 loop
W87
V67
F61
D120
Zn1
Zn2
1b
K224
B1
BcII:1b
C
D120
Zn1
Zn2
IMP-1:1b
IMP-1:native
D
D120
Zn1
Zn2
BcII:1b
BcII:native

Figure 8

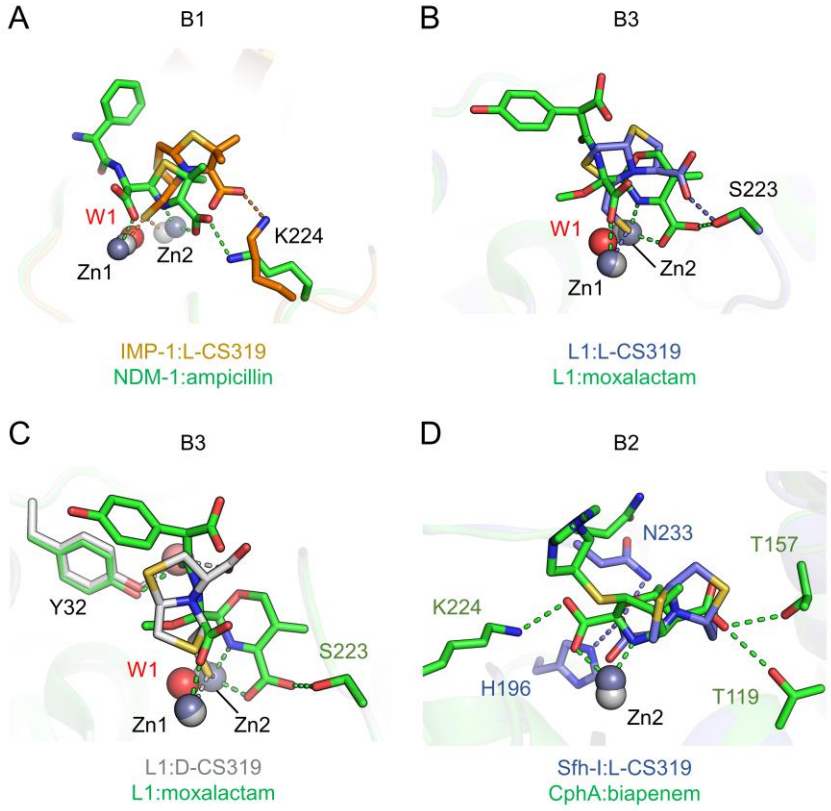
A
B1
W1
Zn1
Zn2
K224
IMP-1:L-CS319
NDM-1:ampicillin
B
B3
S223
W1
Zn1
Zn2
L1:L-CS319
L1:moxalactam
C
B3
Y32
S223
W1
Zn1
Zn2
L1:D-CS319
L1:moxalactam
D
B2
N233
T157
K224
H196
T119
Zn2
Sfh-I:L-CS319
CphA:biapenem

Figure 9

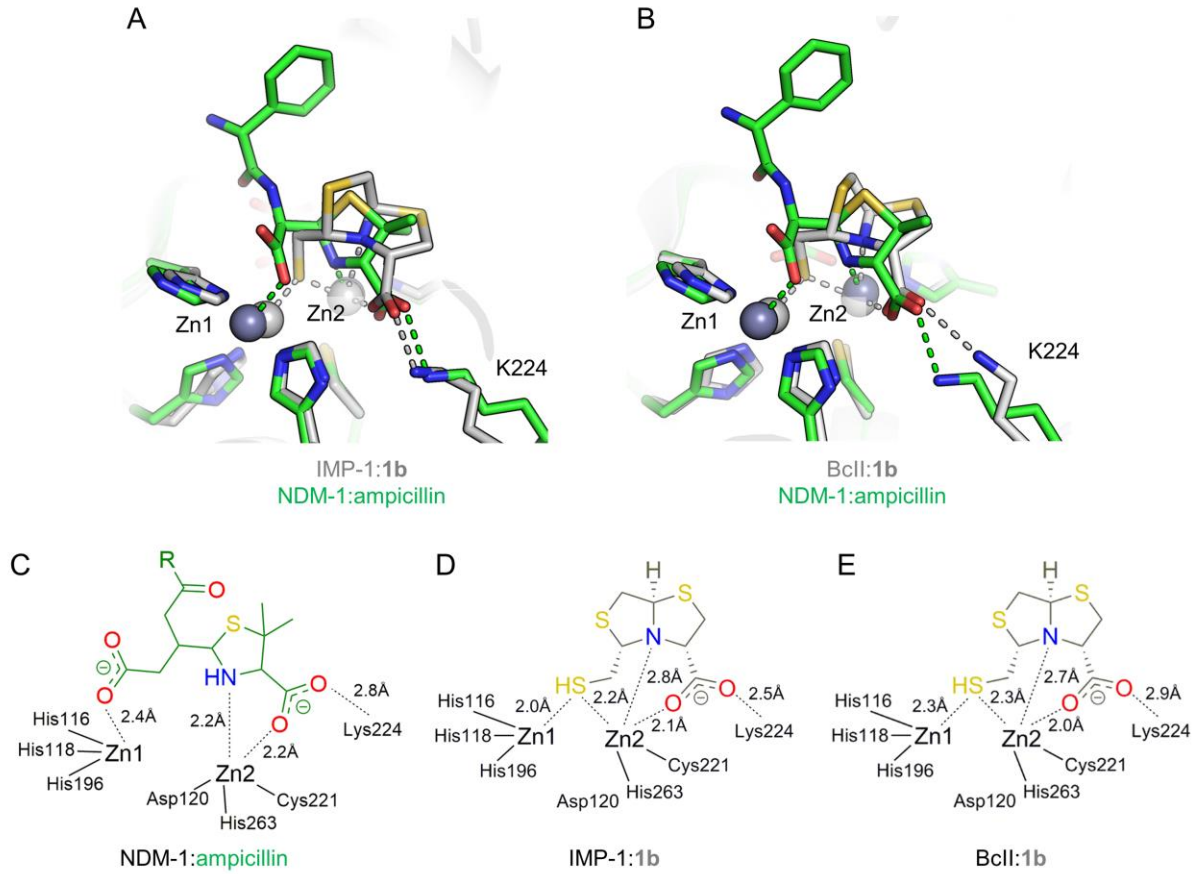
A
Zn1
Zn2
K224
IMP-1:1b
NDM-1:ampicillin
B
Zn1
Zn2
K224
BcII:1b
NDM-1:ampicillin
C
R
O
S
HN
O
2.8Å
Lys224
His116
2.4Å
2.2Å
His118
Zn1
2.2Å
His196
Zn2
Asp120
Cys221
His263
NDM-1:ampicillin
D
H
S
S
N
HS
2.8Å
O
2.5Å
His116
2.0Å
2.2Å
O
His118
Zn1
Zn2
2.1Å
Lys224
His196
Cys221
Asp120
His263
IMP-1:1b
E
H
S
S
N
HS
2.7Å
O
2.9Å
His116
2.3Å
2.3Å
O
His118
Zn1
Zn2
2.0Å
Lys224
His196
Cys221
Asp120
His263
BcII:1b

Table 1. *In vitro* competitive inhibition of MBLs by bisthiazolidines

MBL subclass	Enzyme	Substrate	Inhibition constants (K_i / μM)				
			1a	**1b**	**2a**	**2b**	**Reference**
B1	NDM-1	Imipenem	7 ± 1	19 ± 3	18 ± 3	12 ± 1	(17)
	VIM-2	Imipenem	3.7 ± 0.3	5.4 ± 0.4	3.8 ± 0.2	14 ± 1	(18)
	IMP-1	Imipenem	8 ± 2	6 ± 1	15 ± 3	14 ± 3	-
	BcII	Imipenem	36 ± 2	53 ± 5	32 ± 3	84 ± 6	-
B2	Sfh-I	Imipenem	0.26 ± 0.03	26 ± 3	0.36 ± 0.04	29 ± 3	-
B3	L1	Imipenem	12 ± 1	10 ± 1	11 ± 2	10 ± 1	-
	GOB-18	Imipenem	41 ± 4	30 ± 2	31 ± 2	10 ± 1	-

Supporting Information

SI Results

High resolution crystal structure of native, uncomplexed di-zinc IMP-1

At 3.1 Å, in space group P21 [one molecule in the asymmetric unit (ASU)], PDB 1DDK represented the highest resolution structure of uncomplexed di-zinc IMP-1. At this resolution, it was not possible to model important features such as the nucleophilic water. We therefore sought to obtain a high resolution structure of uncomplexed di-zinc IMP-1.

We have solved the structure of native di-zinc IMP-1 in the same space group and cell dimensions ($P2_12_12_1$, 4 molecules in the ASU) as the BTZ:IMP-1 complexes, allowing direct comparison between structures. Resolution extended to 1.98 Å (**Table S1**) and the model includes residues (standard BBL numbering) 38-298 (chain A, average B-factor 34.3 $Å^2$), 36-298 (chain B, average B-factor 35.1 $Å^2$), 39-302 (chain C, average B-factor 34.9 $Å^2$), 39-298 (chain D, average B-factor 53.0 $Å^2$). Chain B also includes the N-terminal residues G and P, left over after 3C protease cleavage of the hexa-histidine tag. The quality of the density allowed modelling of the nucleophilic water in all four chains (B-factors 26.6 $Å^2$, 25.7 $Å^2$, 23.74 $Å^2$ and 30.46 $Å^2$, chains A-D, respectively), and confident placement of the L3 loop (residues 61-65) with B-factors 56.2 $Å^2$, 37.1 $Å^2$, 40.8 $Å^2$ and 64.1 $Å^2$ (chains A-D, respectively).

Uncomplexed di-zinc IMP-1 has the same overall fold as the previous IMP-1 structure (PDB 1DDK) with RMSDs 0.52 Å (chain A, over 218 Cα atoms), 0.58 Å (B, 218), 0.63 Å (C, 217) and 0.47 Å (D, 217). Zn1-Zn2 distances (± 0.19 Å) are 3.42 Å (chain A), 3.36 Å (B), 3.34 Å (C), 3.37 Å (D) compared to 1DDK Zn1-Zn2 3.29 Å (± 0.65 Å). The nucleophilic water bridges the active-site zincs and over the four chains has refined consistently closer (± 0.19 Å) to Zn2 (1.87 Å, 1.93 Å, 1.91 Å and 1.85 Å) than Zn1 (2.43 Å, 2.17 Å, 2.11 Å, 2.26 Å), with a second water molecule liganding Zn2 (2.27 Å, chain A). This results in tetrahedral (Zn1) and distorted trigonal byprimidal (Zn2) zinc geometries, common to B1 MBLs.

Confirming the flexible nature of the L3 loop, it adopts a different conformation in chain C compared to chains A, B and D where it is present in a more ‘open’ conformation than the three other chains (a *c.* 5 Å shift, **Figure S11**). This could be due to the fact the L3 loop forms extensive crystal contacts between neighbouring molecules in the ASU, resulting in similar L3 loop B-factors to the protein main chain (particularly for chains B and C).

SI Figures

Figure S1

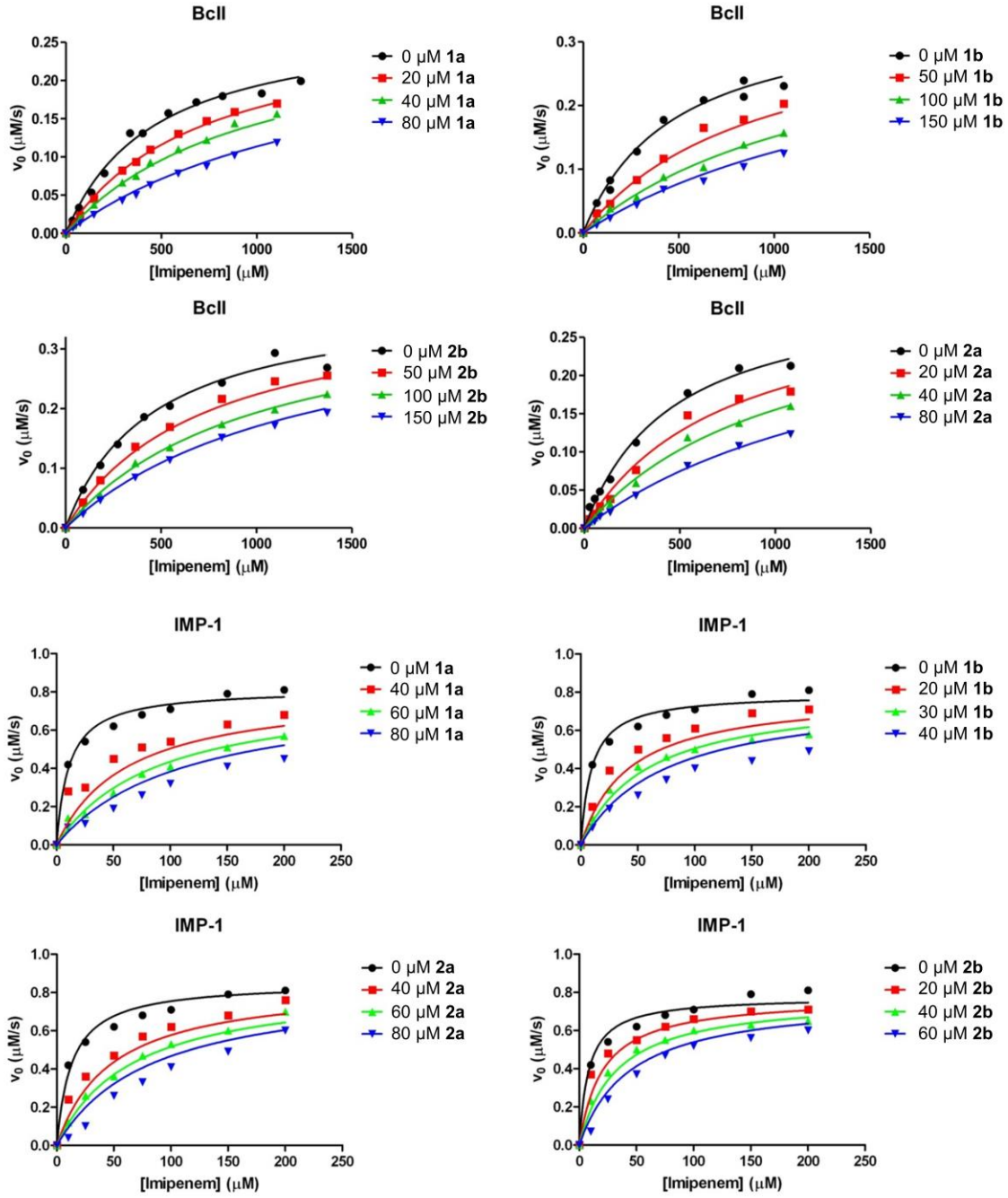

Figure S2

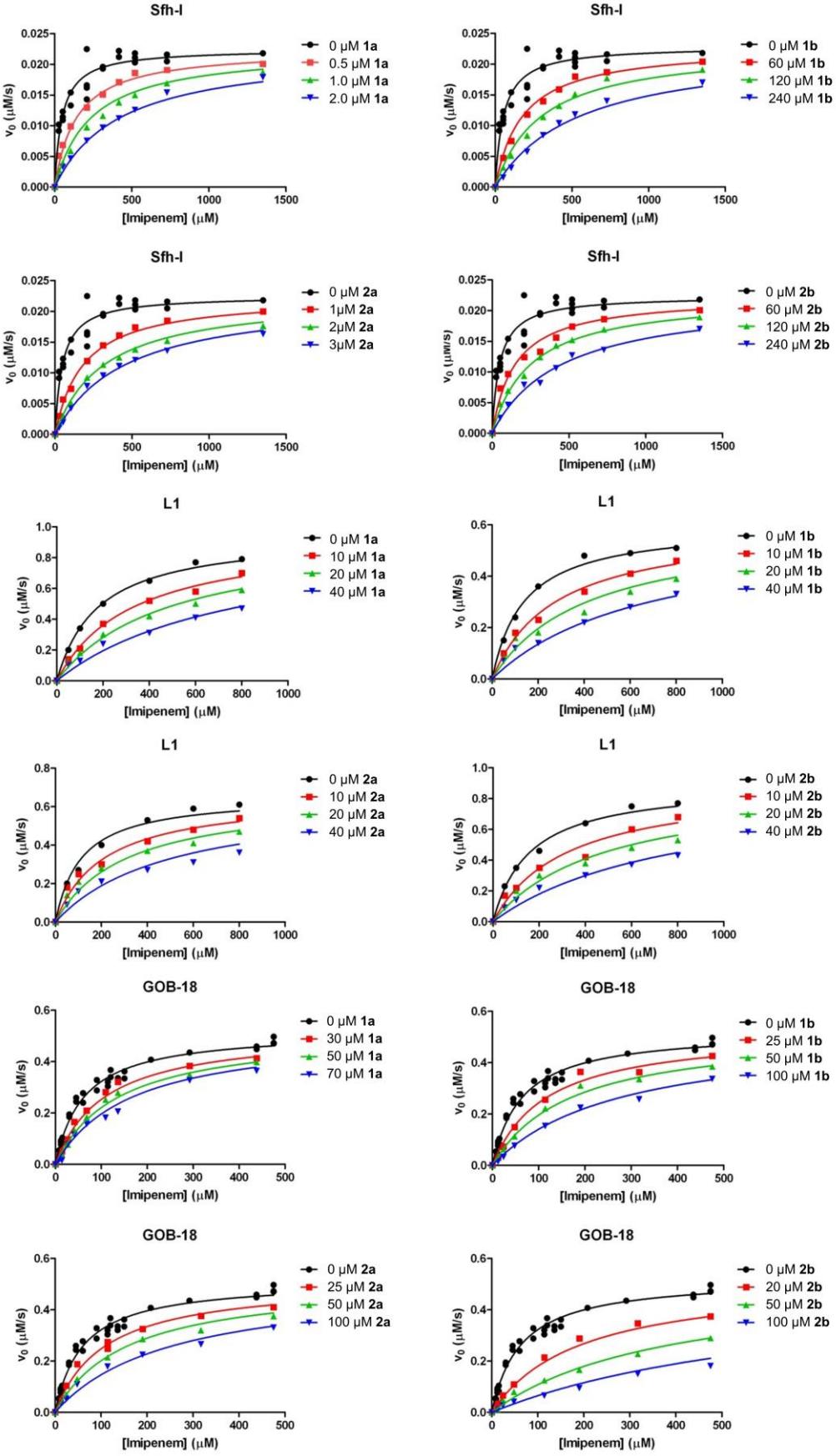
Sfh-I
0 μM 1a
0.5 μM 1a
1.0 μM 1a
2.0 μM 1a
Sfh-I
0 μM 1b
60 μM 1b
120 μM 1b
240 μM 1b
Sfh-I
0 μM 2a
1μM 2a
2μM 2a
3μM 2a
Sfh-I
0 μM 2b
60 μM 2b
120 μM 2b
240 μM 2b
L1
0 μM 1a
10 μM 1a
20 μM 1a
40 μM 1a
L1
0 μM 1b
10 μM 1b
20 μM 1b
40 μM 1b
L1
0 μM 2a
10 μM 2a
20 μM 2a
40 μM 2a
L1
0 μM 2b
10 μM 2b
20 μM 2b
40 μM 2b
GOB-18
0 μM 1a
30 μM 1a
50 μM 1a
70 μM 1a
GOB-18
0 μM 1b
25 μM 1b
50 μM 1b
100 μM 1b
GOB-18
0 μM 2a
25 μM 2a
50 μM 2a
100 μM 2a
GOB-18
0 μM 2b
20 μM 2b
50 μM 2b
100 μM 2b
v0 (μM/s)
[Imipenem] (μM)

Figure S3

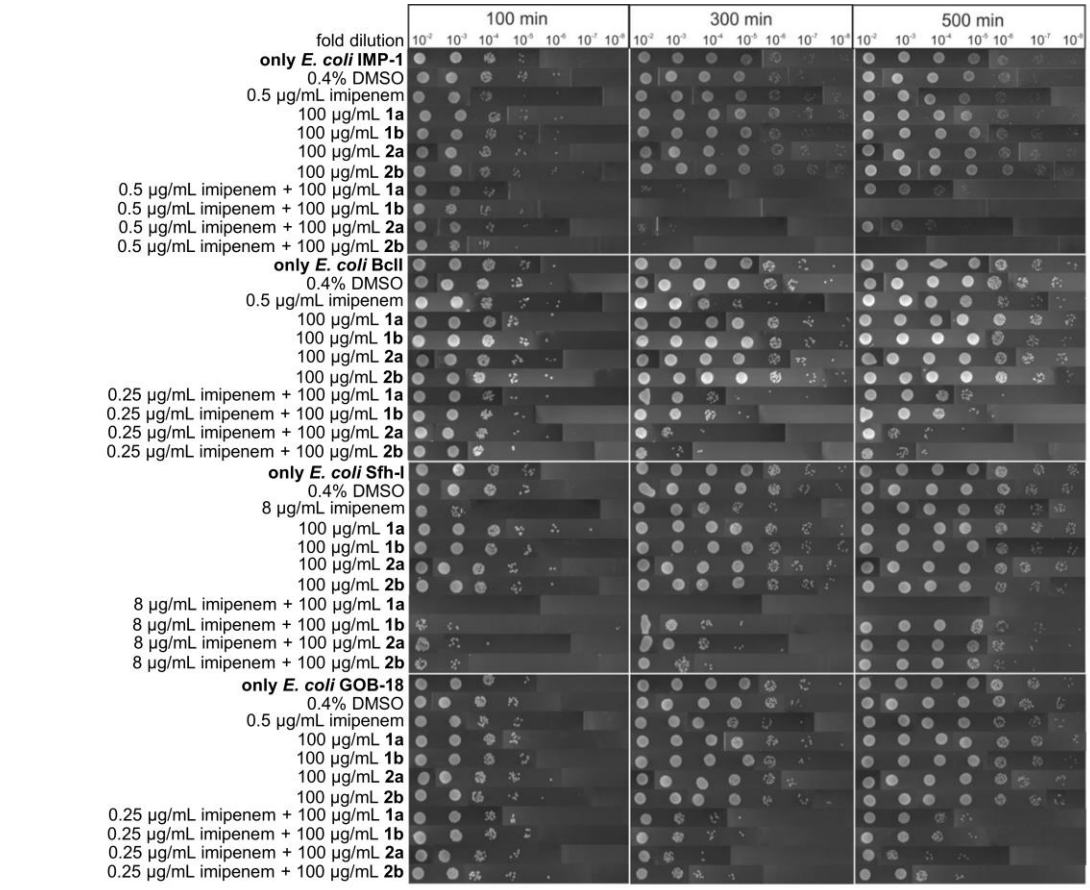
100 min
300 min
500 min
fold dilution
only E. coli IMP-1
0.4% DMSO
0.5 µg/mL imipenem
100 µg/mL 1a
100 µg/mL 1b
100 µg/mL 2a
100 µg/mL 2b
0.5 µg/mL imipenem + 100 µg/mL 1a
0.5 µg/mL imipenem + 100 µg/mL 1b
0.5 µg/mL imipenem + 100 µg/mL 2a
0.5 µg/mL imipenem + 100 µg/mL 2b
only E. coli BcII
0.4% DMSO
0.5 µg/mL imipenem
100 µg/mL 1a
100 µg/mL 1b
100 µg/mL 2a
100 µg/mL 2b
0.25 µg/mL imipenem + 100 µg/mL 1a
0.25 µg/mL imipenem + 100 µg/mL 1b
0.25 µg/mL imipenem + 100 µg/mL 2a
0.25 µg/mL imipenem + 100 µg/mL 2b
only E. coli Sfh-I
0.4% DMSO
8 µg/mL imipenem
100 µg/mL 1a
100 µg/mL 1b
100 µg/mL 2a
100 µg/mL 2b
8 µg/mL imipenem + 100 µg/mL 1a
8 µg/mL imipenem + 100 µg/mL 1b
8 µg/mL imipenem + 100 µg/mL 2a
8 µg/mL imipenem + 100 µg/mL 2b
only E. coli GOB-18
0.4% DMSO
0.5 µg/mL imipenem
100 µg/mL 1a
100 µg/mL 1b
100 µg/mL 2a
100 µg/mL 2b
0.25 µg/mL imipenem + 100 µg/mL 1a
0.25 µg/mL imipenem + 100 µg/mL 1b
0.25 µg/mL imipenem + 100 µg/mL 2a
0.25 µg/mL imipenem + 100 µg/mL 2b

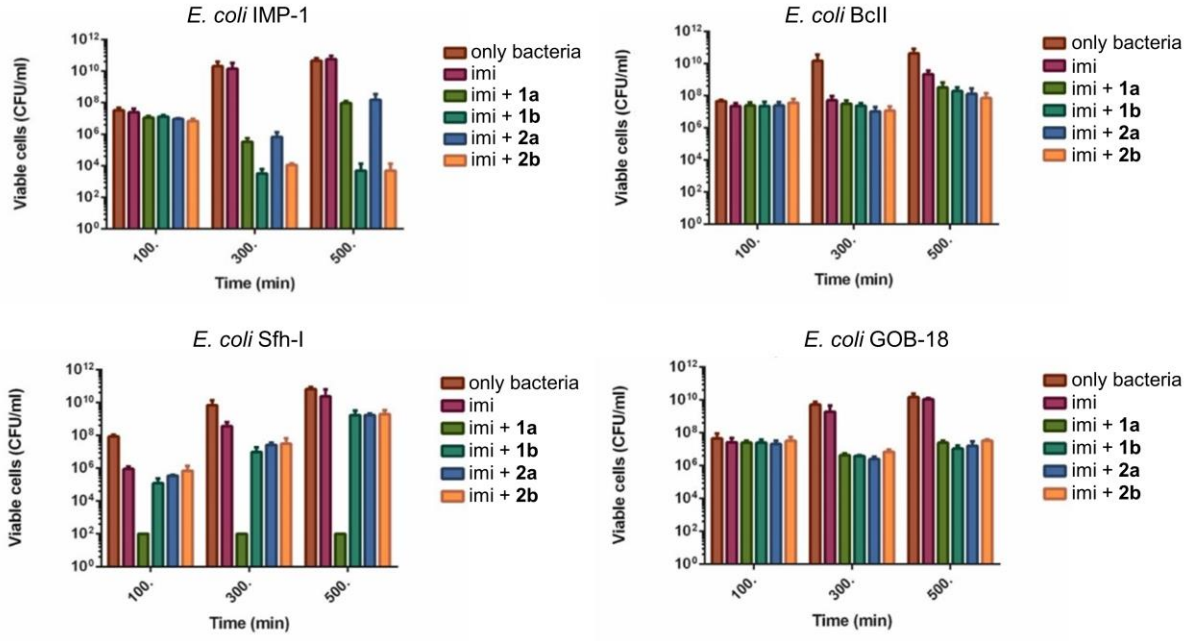
E. coli IMP-1
E. coli BcII
E. coli Sfh-I
E. coli GOB-18
Viable cells (CFU/ml)
Time (min)
only bacteria
imi
imi + 1a
imi + 1b
imi + 2a
imi + 2b

Figure S4

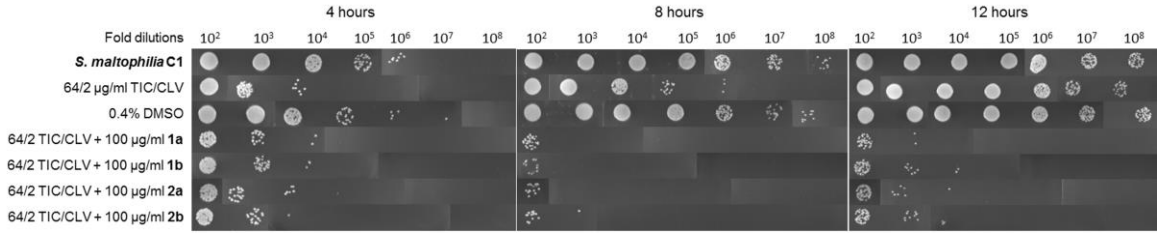
4 hours
8 hours
12 hours
Fold dilutions
10² 10³ 10⁴ 10⁵ 10⁶ 10⁷ 10⁸
S. maltophilia C1
64/2 µg/ml TIC/CLV
0.4% DMSO
64/2 TIC/CLV + 100 µg/ml 1a
64/2 TIC/CLV + 100 µg/ml 1b
64/2 TIC/CLV + 100 µg/ml 2a
64/2 TIC/CLV + 100 µg/ml 2b

Figure S5

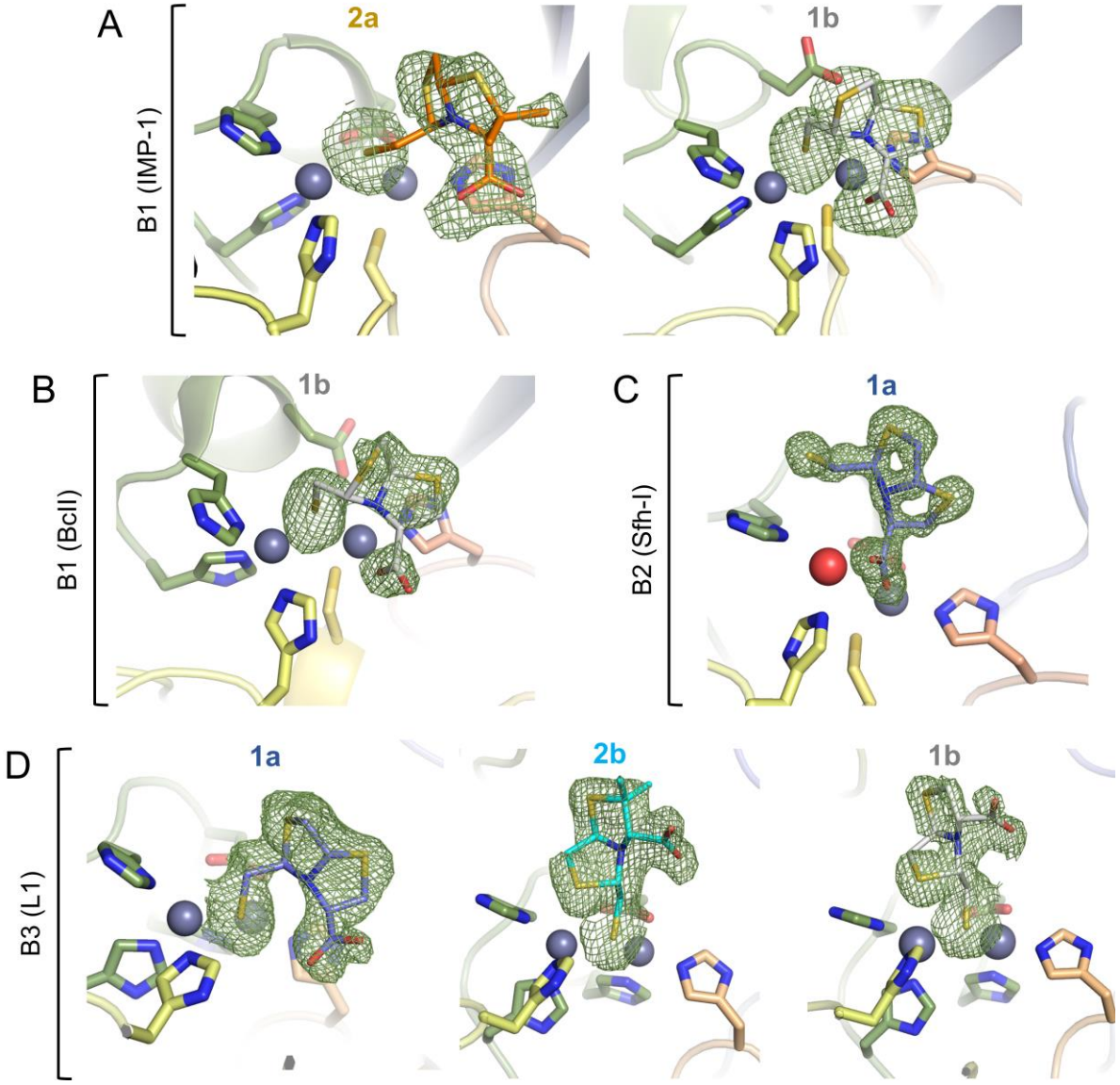

Figure S6

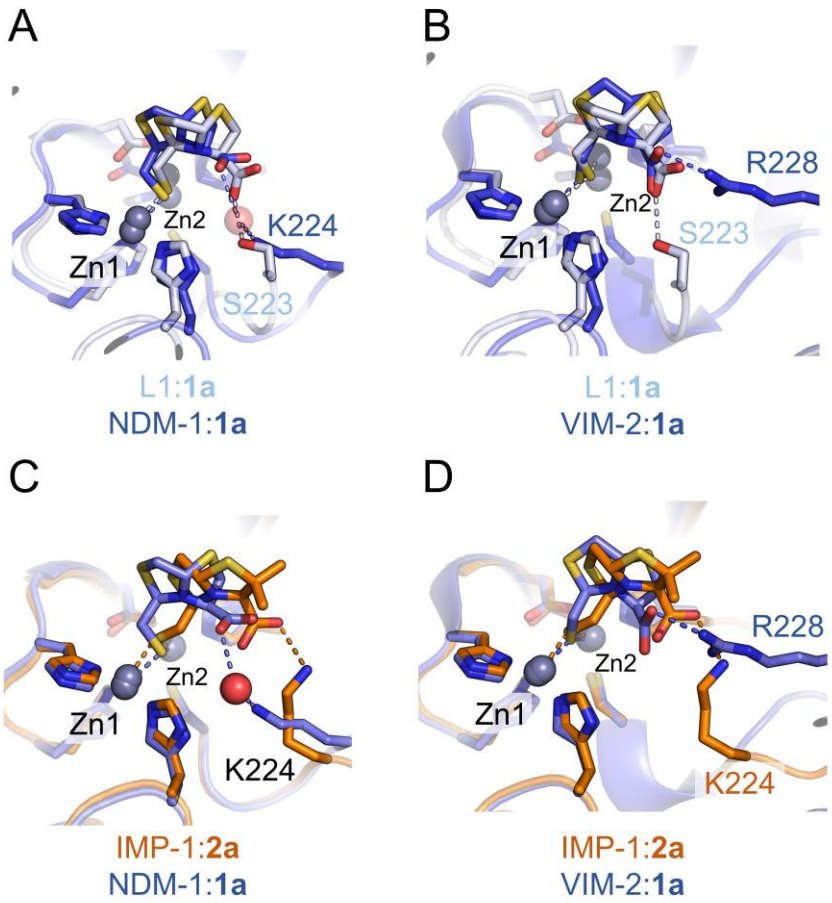
A
Zn2
K224
Zn1
S223
L1:1a
NDM-1:1a
B
R228
Zn2
S223
Zn1
L1:1a
VIM-2:1a
C
Zn2
Zn1
K224
IMP-1:2a
NDM-1:1a
D
R228
Zn2
Zn1
K224
IMP-1:2a
VIM-2:1a

Figure S7

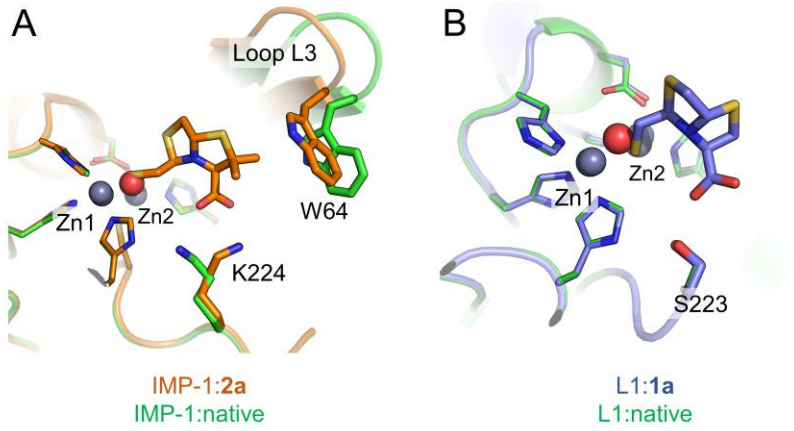
A
Loop L3
Zn1
Zn2
W64
K224
IMP-1:2a
IMP-1:native
B
Zn2
Zn1
S223
L1:1a
L1:native

Figure S8

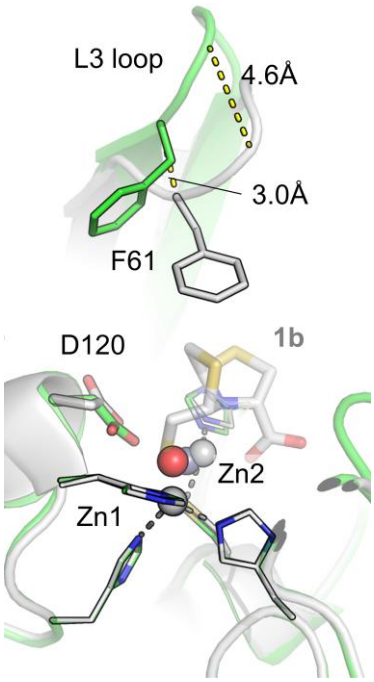

Figure S9

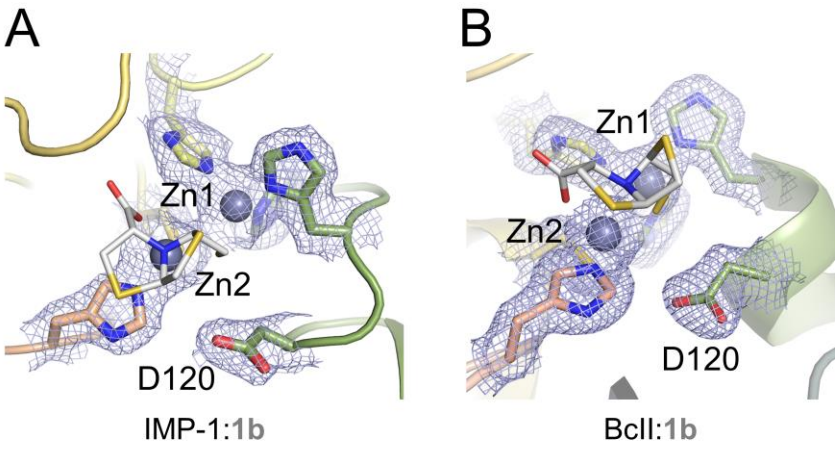

Figure S10

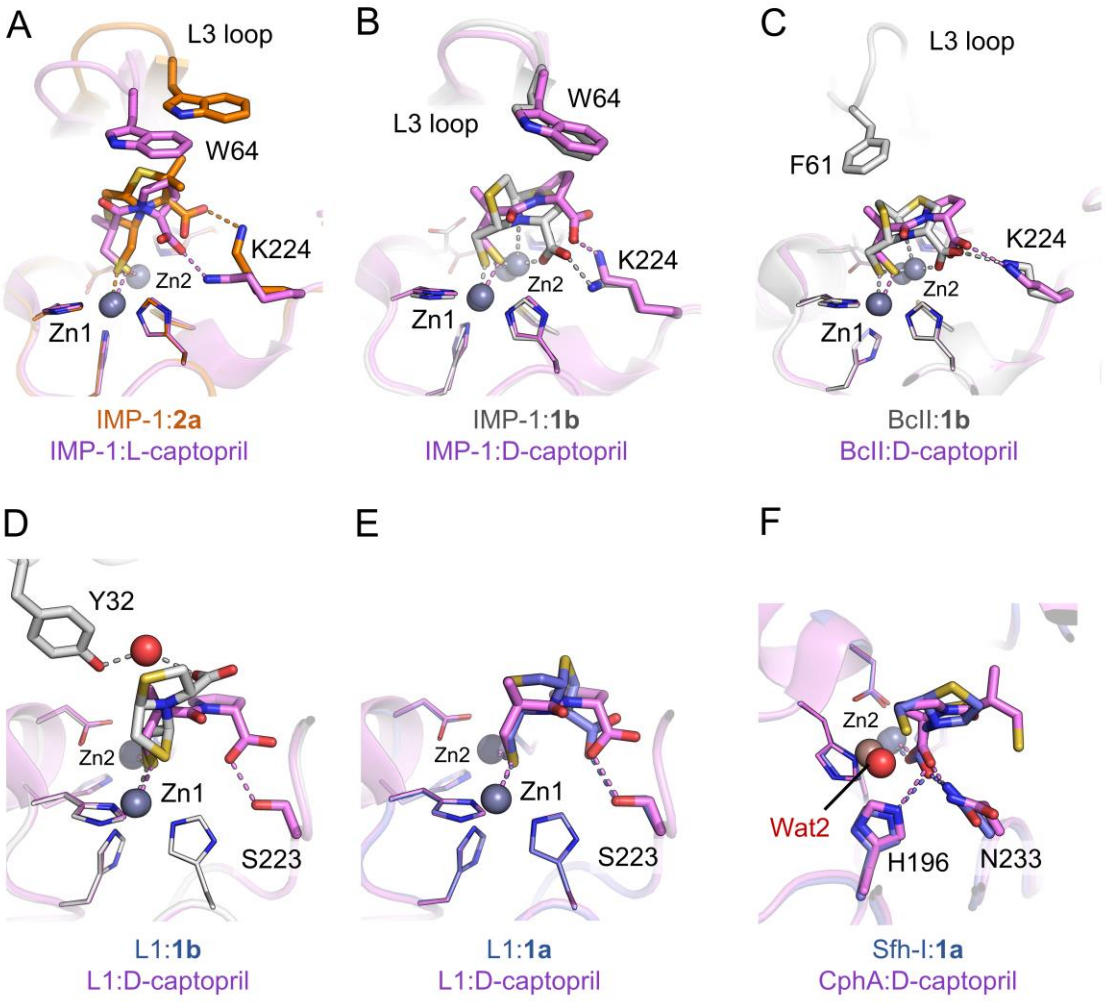
A
L3 loop
W64
K224
Zn2
Zn1
IMP-1:2a
IMP-1:L-captopril
B
L3 loop
W64
K224
Zn2
Zn1
IMP-1:1b
IMP-1:D-captopril
C
L3 loop
F61
K224
Zn2
Zn1
BcII:1b
BcII:D-captopril
D
Y32
Zn2
Zn1
S223
L1:1b
L1:D-captopril
E
Zn2
Zn1
S223
L1:1a
L1:D-captopril
F
Zn2
Wat2
H196
N233
Sfh-I:1a
CphA:D-captopril

Figure S11

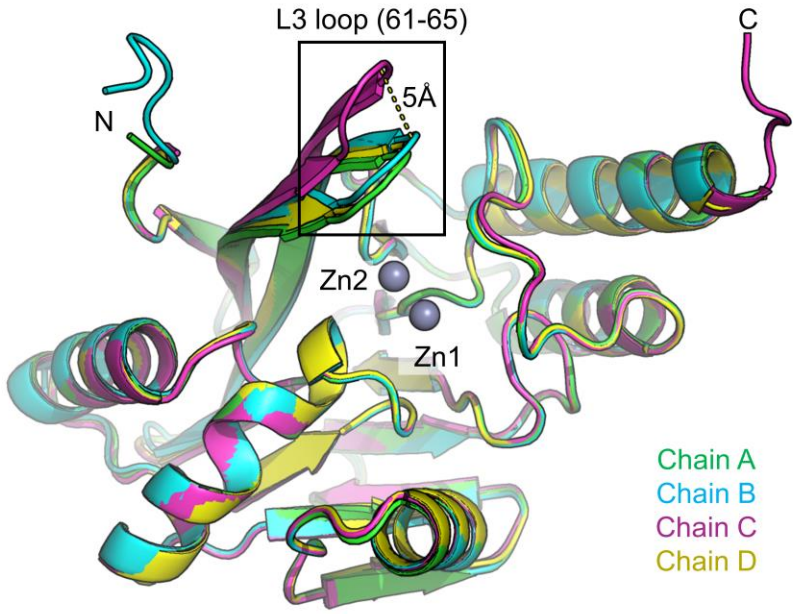

SI Tables

Table S1. Data collection and refinement statistics.

MBL	**IMP-1**			**BcII**	**Sfh-I**	**L1**		
MBL class	**B1**			**B1**	**B2**	**B3**		
Inhibitor	**1b**	**2a**	**un-complexed**	**1b**	**1a**	**1a**	**1b**	**2b**
Data collection								
Space group	$P2_12_12_1$	$P2_12_12_1$	$P2_12_12_1$	$C2_1$	$P2_1$	$P6_422$	$P6_422$	$P6_422$
Molecules/ASU	4	4	4	1	2	1	1	1
Cell dimensions								
a, *b*, *c* (Å)	48.56, 77.70, 261.89	49.05, 78.45, 260.61	49.19, 78.00, 260.13	53.08, 61.28, 69.51	32.77, 86.70, 72.23	104.98, 104.98, 98.47	104.96, 104.96, 98.83	105.13, 105.13, 98.17
α, β, γ (°)	90.0, 90.0, 90.0	90.0, 90.0, 90.0	90.0, 90.0, 90.0	90.0, 93.04, 90.0	90.0, 90.09, 90.0	90.0, 90.0, 120.0	90.0, 90.0, 120.0	90.0, 90.0, 120.0
Wavelength	0.9686	0.92	0.96862	1.5418	0.97949	0.97623	0.9686	0.97949
Resolution (Å)*	37.24 – 2.30 (2.38 – 2.30)	29.82 – 2.30 (2.38 – 2.30)	35.57 – 1.98 (2.03 – 1.98)	40.09 - 1.80 (1.86-1.80)	19.42 – 1.30 (1.32 – 1.30)	30.87 – 1.63 (1.66 – 1.627)	28.97 – 1.84 (1.88 – 1.84)	30.35 – 1.8 (1.84 – 1.80)
R_{merge}	0.190 (1.530)	0.109 (0.521)	0.200 (0.779)	0.272 (0.760)	0.118 (0.413)	0.084 (0.65)	0.213 (0.778)	0.180 (0.858)
I / σI	11.60 (3.10)	18.3 (4.2)	5.8 (2.2)	4.0 (1.30)	7.6 (3.6)	41.04 (6.0)	16.9 (5.6)	21.69 (4.29)
Completeness (%)	100 (99.8)	99.9 (99.9)	99.0 (98.0)	97.8 (81.7)	97.6 (95.5)	99.7 (94.1)	99.4 (90.3)	100 (100)
Redundancy	17.7 (18.1)	10.3 (9.9)	9.5 (8.3)	4.2 (2.7)	5.8 (5.9)	65.3 (27.3)	37.9 (32.2)	33.8 (34.9)
Refinement								
Resolution (Å)	37.24 – 2.30 (2.35 – 2.30)	29.82 – 2.30 (2.35 – 2.30)	35.57 – 1.98 (2.01 – 1.98)	40.09 – 1.80 (1.85 – 1.80)	19.42 – 1.30 (1.33 – 1.30)	30.87 – 1.63 (1.67 – 1.63)	28.97 – 1.84 (1.91 – 1.84)	30.35 – 1.80 (1.86 – 1.80)
No. reflections	45125	45814	69452	19247	91618	40522	28142	30208
R_{work} / R_{free}	17.77 (23.76) / 22.03 (26.90)	18.20 (24.06) / 22.20 (26.00)	17.21 (24.55) / 20.45 (27.52)	19.3 (38.40) / 24.4 (43.10)	16.02 (27.20) / 18.86 (30.50)	15.74 (21.86) / 18.18 (24.26)	14.79 (20.27) / 19.49 (26.11)	16.55 (25.07) / 19.57 (25.50)
Coordinate error (Å)[1]	0.26	0.23	0.19	0.13	0.03	0.14	0.17	0.18
No. atoms								
Protein	6888	6870	6892	1718	3717	2012	2006	2015
Solvent/Zn	338	337	510	140	605	340	337	283
Inhibitor	52 (4)	45 (3)	-	13 (1)	26 (2)	13 (1)	13 (1)	15 (1)
B-factors								
Protein	43.45	39.66	39.64	28.71	11.02	25.72	21.64	25.15
Solvent/Zn	42.17	37.88	44.52	34.64	20.74	38.94	36.0	36.4
Inhibitor	44.00	66.74	-	45.32	13.73	54.02	38.45	42.98
R.m.s. deviations								
Bond lengths (Å)	0.009	0.008	0.008	0.017	0.0110	0.016	0.007	0.008
Bond angles (°)	1.18	1.18	1.12	1.871	1.5689	1.573	1.04	1.05
Ramchandran (%)								
Outliers	0.0	0.0	0.5	0.32	0.4	0.0	0.0	0.0
Favoured	97.7	97.2	97.4	96.43	97.0	96.4	96.4	95.6

*Values in parentheses correspond to the highest-resolution shell

[1]Maximum-likelihood coordinate error

Table S2. Ligand validation statistics

Protein	MBL subclass	Chain	Ligand	LLDF[1]	RSR[2]	RSCC[3]
IMP-1	B1	C	**1b**	-1.41	0.08	0.991
IMP-1	B1	C	**2a**	0.15	0.15	0.962
BcII	B1	N/A	**1b**	0.36	0.13	0.930
Sfh-I	B2	A	**1a**	0.19	0.06	0.949
L1	B3	N/A	**1a**	1.88	0.16	0.924
L1	B3	N/A	**1b**	3.44	0.18	0.918
L1	B3	N/A	**2b**	1.24	0.15	0.951

[1]Local ligand density fit as reported by PDB validation

[2]Real space R-value as reported by PDB validation

[3]Real-space density correlation coefficient as reported by Phenix

Table S3. Zinc distances in B1 and B3 MBL active sites.

		Distances (Å)				
			BTZ-SH to		Nucleophilic water to	
Protein	**Ligand**	**Zn1-Zn2**	**Zn1**	**Zn2**	**Zn1**	**Zn2**
IMP-1	Native[3]	3.34	-	-	2.11	1.91
	1b[4]	3.64	2.31	2.28	-	-
	2a[4]	3.67	2.43	2.26	-	-
L1	Native[1]	3.46	-	-	1.88	2.06
	1b	3.89	2.37	2.04	-	-
	1a	3.86	2.27	2.22	-	-
	2b	3.80	2.34	1.96	-	-
BcII	Native[2]	3.50	-	-	2.33	2.34
	1b	3.80	1.95	1.99	-	-

[1]PDB 1SML
[2]PDB 4C09
[3]Chain C
[4]Chain A